1·0    2·8    2·5
       5·0  3·15   2·2
            3·5
1·1         4·0    2·0
            4·5
                   1·8
1·25   1·4   1·6

NATIONAL BUREAU OF STANDARDS
MICROCOPY RESOLUTION TEST CHART

# AD-A158 733

AFWAL-TR-85-2022

METASTABLE INTERACTIONS:  DISSOCIATIVE EXCITATION

L.D. SCHEARER

PHYSICS DEPARTMENT
UNIVERSITY OF MISSOURI-ROLLA
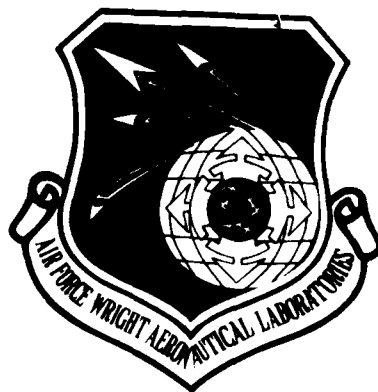ROLLA, MISSOURI  65401

MAY 1985

FINAL REPORT FOR PERIOD AUGUST 1981 – JANUARY 1985

DTIC FILE COPY

DTIC
SELECTE
AUG 2 9 1985
S     D

G

85 - 8 20 051

ALAN GARSCADDEN, Research Physicist
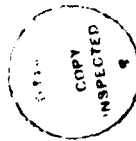Power Components Branch
Aerospace Power Division
Aero Propulsion Laboratory

PAUL R. BERTHEAUD, Chief
Power Components Branch
Aerospace Power Division
Aero Propulsion Laboratory

FOR THE COMMANDER

JAMES D. REAMS
Chief, Aerospace Power Division
Aero Propulsion Laboratory

# REPORT DOCUMENTATION PAGE

| 1a. REPORT SECURITY CLASSIFICATION<br>Unclassified | 1b. RESTRICTIVE MARKINGS |
|---|---|
| 2a. SECURITY CLASSIFICATION AUTHORITY | 3. DISTRIBUTION/AVAILABILITY OF REPORT<br>Approved for public release; distribution unlimited. |
| 2b. DECLASSIFICATION/DOWNGRADING SCHEDULE | |
| 4. PERFORMING ORGANIZATION REPORT NUMBER(S)<br>AFWAL-TR-85-2022 | 5. MONITORING ORGANIZATION REPORT NUMBER(S)<br>AFWAL-TR-85-2022 |

| 6a. NAME OF PERFORMING ORGANIZATION<br>University of Missouri-Rolla | 6b. OFFICE SYMBOL (If applicable) | 7a. NAME OF MONITORING ORGANIZATION<br>Aero Propulsion Laboratory (AFWAL/POOC)<br>Air Force Wright Aeronautical Laboratories |
|---|---|---|
| 6c. ADDRESS (City, State and ZIP Code)<br>Physics Department<br>University of Missouri-Rolla<br>Rolla, Missouri 65401 | | 7b. ADDRESS (City, State and ZIP Code)<br>Air Force Systems Command<br>Wright-Patterson Air Force Base OH 45433 |

| 8a. NAME OF FUNDING/SPONSORING ORGANIZATION<br>Power Components Branch | 8b. OFFICE SYMBOL (If applicable)<br>AFWAL/POOC-3 | 9. PROCUREMENT INSTRUMENT IDENTIFICATION NUMBER<br>F33615-81-K-2081 |
|---|---|---|

8c. ADDRESS (City, State and ZIP Code)
Air Force Wright Aeronautical Laboratories
Wright-Patterson AFB OH 45433

10. SOURCE OF FUNDING NOS.

| PROGRAM ELEMENT NO. | PROJECT NO. | TASK NO. | WORK UNIT NO. |
|---|---|---|---|
| 2301 | S2 | 89 | 2301S289 |

11. TITLE (Include Security Classification)
Metastable Interactions: Dissociative Excitation 6110 1 F

12. PERSONAL AUTHOR(S)
L. D. Schearer

| 13a. TYPE OF REPORT<br>Final | 13b. TIME COVERED<br>FROM Aug 81 TO Jan 85 | 14. DATE OF REPORT (Yr., Mo., Day)<br>May 1985 | 15. PAGE COUNT<br>79 |
|---|---|---|---|

16. SUPPLEMENTARY NOTATION

| 17. COSATI CODES | | | 18. SUBJECT TERMS (Continue on reverse if necessary and identify by block number) |
|---|---|---|---|
| FIELD | GROUP | SUB. GR. | →Energy Transfer, Collisions, Radiation, Metastables |
| | | | |
| | | | |

19. ABSTRACT (Continue on reverse if necessary and identify by block number)
The work reported here is concerned with the interaction between thermal energy metastable atoms and molecules and other atoms and molecules in a beam or in a flowing afterglow. The importance of reactions involving metastable species can be traced to the relative ease with which energy can be stored in ensembles of metastable atoms and molecules and the wide variety of reactions in which they can participate. Of particular interest are those processes which involve energy transfer from the metastable system to a second species which results in excited states which fluoresce. Two principal experimental methods have been used: (a) Metastable beams crossed with a target species, (b) Fast flowing rare gas and nitrogen afterglows. A wide variety of metal halogen, Group II metals, methane and silane have been reacted with helium, argon and nitrogen metastables. Originator

 ... the keywords include:

| 20. DISTRIBUTION/AVAILABILITY OF ABSTRACT<br>UNCLASSIFIED/UNLIMITED ☒ SAME AS RPT. ☐ DTIC USERS ☐ | 21. ABSTRACT SECURITY CLASSIFICATION<br>Unclassified |
|---|---|

| 22a. NAME OF RESPONSIBLE INDIVIDUAL<br>ALAN GARSCADDEN | 22b. TELEPHONE NUMBER (Include Area Code)<br>52923/53835 | 22c. OFFICE SYMBOL<br>AFWAF/POOC-3 |
|---|---|---|

# CONTENTS

# METASTABLE ATOM/MOLECULE INTERACTIONS

## I. Interactions in Beams

### Introduction

The work reported here is concerned with the interaction between thermal energy metastable atoms and molecules and other atoms and molecules in a beam or in a flowing afterglow. The importance of reactions involving metastable species can be traced to the relative ease with which energy can be stored in ensembles of metastable atoms and molecules and the wide variety of reactions in which they can participate as shown in Table 1.

### TABLE 1. Metastable Reactions

| Bound-bound | $M^* + XY \rightarrow M + (XY)^*$ | Excitation Transfer |
|---|---|---|
| Transitions | $M^* + A \rightarrow M^{*'} + A$ | Excitation Transfer |
| | $M^* + e \rightarrow M + e + k.e.$ | Superelastic Collisions |
| | $M^* + A \rightarrow (MA)^*$ | Associative Excitation |
| | $M^* + XY \rightarrow M + X^* + Y$ | Dissociative Excitation |
| Bound-free | $M^* + A \quad M + A^+ + e$ | Penning Ionization |
| Transitions | $M^* + A \quad (MA)^+ + e$ | Associative Ionization |
| | $M^* + XY \quad M + X^+ + Y + e$ | Dissociative Ionization |

Of particular interest here are those processes which involve energy transfer from the metastable system to a second species which results in excited states which fluoresce. The interest stems from the fact that such energy transfer processes can lead to population inversions in gaseous systems, i.e. gas lasers.

While much of the interest in metastable interactions has centered on ionizing collisions such as Penning ionization, it is well-known that metastable systems undergo many electronic energy transfer reactions which

3

yield neutral excited products (1). These energy transfer reactions can occur even when the ionization potential of the target species lies well below the energy of the metastable species. Such dissociative excitations are among the least studied elementary processes in which metastable atoms/molecules and target molecules can participate.

The mercuric halide compounds $HgBr_2$, $HgCl_2$, and $HgI_2$ are of recent interest because of laser output achieved on the $B^2\Sigma - X^2\Sigma$ transition in the respective mercuric halide radicals in the range of 400-600 nm. Population inversion has been obtained by photodissociation and electron impact excitation in mixtures o the mercuric-halide compounds and the rare gases. Chang and Burnham (3) have noted improved laser efficiency and improved performance with the added $N_2$ has been attributed to the dissociative excitation of the $HgBr_2$ in the reaction

$$N_2(A^3\Sigma) + HgBr_2 \rightarrow HgBr^*(B^2\Sigma) + Br + N_2(X^1\Sigma)$$

This dissociative excitation process has been studied by Nighan (2) in a fast-pulse discharge and by Chang and Burnham (3) and Setser et al. (4) in a flowing afterglow apparatus. Rate constants for the process have been obtained by using a relatively complicated comparison of the $XeF^*$ to $HgBr^*$ emission. Fahey and Schearer (5) have observed the dissociative excitation process in a vibrationally excited $N_2$ metastable beam.

The dissociative excitation process is also a clever way in which one can obtain large concentrations of free metal atoms having low vapor pressures from a molecular complex which has a high vapor pressure. Thus, for example, Pb, Ge, Ga, Sn, and Sb can be easily studied near room temperature by dissociatively exciting $PbI_2$, $GeI_4$, $GaI_3$, $SnI_2$, and $SbI_3$ by collisions with metastable helium atoms.

We have investigated a variety of metastable interactions with either atomic or molecular metal-bearing compounds. Table 2 summarizes the

investigations reported herein.

Two principal experimental tools have been used in this research program:

(a) Metastable beams crossed with a target species

(b) Fast flowing rare gas and $N_2$ afterglows

The metastable beam apparatus is particularly useful for observation and measurement of elastic scattering cross-sections and total metastable quenching rates due to dissociative excitation and/or Penning ionization. The fast flowing afterglow, with its high density of metastable species, is particularly useful for fluorescence measurements. With these two experimental techniques at our disposal we have been able to observe a wide variety of metastable interactions, again as shown in summary form in Table 2.

# TABLE 2

## METASTABLE INTERACTIONS INVESTIGATED

| Metastable Species | He(M) | Ar(M) | $N_2(M)$ |
|---|---|---|---|
| Target Species | | | |
| $HgBr_2$ | a,d,e | a,d,e | a,d,e |
| $HgCl_2$ | a | a | a,e |
| $HgI_2$ | a | a | a,e |
| Ar | b,d | | |
| Kr | b,d | | |
| Cd | a,b | b | a |
| Zn | a,b | b | a |
| Mg | a | | a |
| Na | | | a,c |
| $PbBr_2$ | a | a* | a* |
| $SbI_3$ | a | a* | a* |
| $CH_4$ | a | | |
| $SiH_4$ | a | | a* |
| $GaI_3$ | a* | a* | a* |
| $GeI_4$ | a* | a* | a* |
| $CdBr_2$ | a | a | a* |
| $CdI_2$ | a | a | a* |
| $N_2$ | a | | |

a*    No fluorescence observed between 6500-2200 Angstoms

a     Fluorescence observed in flowing afterglow

b     Penning cross sections determined

c     Energy transfer

d     Elastic cross sections determined

e     Quenching cross sections determined

## 1. Beam Apparatus and Beam Characterization

The characteristics of the metastable source which provides a flux of $10^{+14} - 10^{+15}$ particles/sec-sr for various particles are shown in Table 3.

### TABLE 3

### METASTABLE BEAM CHARACTERISTICS

| Species | State | Flux (particles/sec-sr) | Velocity (m/sec) | Energy(meV) | E/E(%) |
|---------|-------|-------------------------|------------------|-------------|--------|
| $He^M$ | $^3S_1$ | $3.5 \times 10^{+14}$ | $1.8 \times 10^{+3}$ | 66 meV | 45% |
| $Ne^M$ | $^3P_2$ | $1.5 \times 10^{+14}$ | $8.3 \times 10^{+2}$ | 72 meV | 27% |
| $Ar^M$ | $^3P_2$ | $7.2 \times 10^{+13}$ | $6.0 \times 10^{+2}$ | 74 meV | 27% |
| $N_{2M}$ | $A^3$ | $1.1 \times 10^{+14}$ | $1.1 \times 10^{+3}$ | 180 meV | -- |

## 2. Source Design and Operation

The source is essentially a low-voltage discharge between a sharp needle and cone-shaped skimmer electrode. The discharge is maintained across a pressure gradient creased by differentially pumping a gas nozzle. The source design is shown in Figure 3. A vacuum fitting is mounted in a vacuum wall and seals around a 7 mm OD Pyrex glass tube (A) that extends into the vacuum chamber. A machined piece of boron nitride (B) is attached with epoxy to form a cap for the end of the glass tube. A small hole drilled in this cap serves as the nozzle opening. The skimmer is a cone-shaped piece of stainless steel (C) with a small hole at the apex. Inside the glass tube behind the nozzle, several steel hypodermic needles are supported to lie near the axis of the tube. The skimmer piece is attached with an aluminum gasket to a vacuum wall to allow differential pumping of the source. Gas is admitted to the glass tube by a micrometer leak valve mounted outside of the vacuum chamber. The source region is contained inside a 10 cm Corning Pyrex glass cross which is evacuated by a 300 $ls^{-1}$ oil diffusion pump. The reaction region is a 97 I stainless-

steel chamber in which the pressure is maintained below $1.3 \times 10^4$ Pa ($10^{-6}$ Torr).

The needles behind the nozzle are the cathode of the electric discharge and hence are maintained at a negative potential with respect to the skimmer which is kept at ground potential. Since the needle electrode is a cold-cathode type, the application of the voltage necessary to sustain the discharge is not generally sufficient to initiate a discharge. It is therefore necessary to apply an initiating high-voltage pulse simultaneously with a negative DC sustaining voltage in order to turn on the source. The DC source discharge after initiation by the high voltage pulse is maintained at 3 mA and 400 V.

The optimum nozzle pressures for the three source gases used were measured with a Wallace and Tiernan dial gauge to be 6.7 kPa (50 Torr) for He, 11.3 kPa (85 Torr) for Ne, and 6.0 kPa (45 Torr) for Ar. The background pressure in the source region at these operating pressures was measured with an ionization gauge at low emission current to be between 0.13 and 0.20 Pa (1.0 and 1.5 mTorr). At 0.13 Pa helium background pressure the mass flow rate was determined to be 66 Pals$^{-1}$. The beam flux is a slowly varying function of operating nozzle pressure. At 2.7-6.6 kPa (20-50 Torr) below optimum pressure the source discharge cannot be sustained, and at 6.7-13.3 kPa above optimum pressure the beam flux is reduced to zero after slowly decreasing from the optimum value.

The stability of the source output at 3 mA emission was very good. Degradation in source yield from use results primarily from wearing of the nozzle opening. After a run period of a month at several hours a day, the nozzle diameter is virtually unchanged as measured with a travelling microscope.

### 3. Beam Diagnostics

The beam was characterized using two very different detection methods. The first method of detecting the beam made use of particle detectors. The second method used the detection of optical emission resulting from the interaction of the beam components with a strontium vapour target. Two types of particle detectors were used to observe all beam components and to estimate the absolute flux and energy of the components. For all diagnostic measurements, the beam was kept free of charged species by maintaining an adequate voltage on a set of parallel sweep plates mounted after the skimmer.

### 4. Particle Detection

For direct particle detection, both a *cooper-beryllium particle multiplier* and a specially designed metastable detector were used. Copper-beryllium dynodes have shown better than 50% efficiency for secondary electron by slow metastables and up to 20% efficiency for photons below 200 nm. (See Table 4.) The surface is also sensitive to fast neutral ground state particles and ions of sufficient kinetic energy. The particle multiplier was used with a chopper wheel to analyze the time-of-flight (TOF) spectrum for different component species and their respective velocities. The multiplier was mounted in the chamber such that it could undergo displacements of up to 60 cm in order to allow accurate measurements.

# TABLE 4

## SECONDARY ELECTRON YIELDS FOR AUGER ELECTRON FROM A

## CU-Be-O SURFACE BY THERMAL METASTABLES

| Species | Yield $\gamma_m$ |
|---|---|
| *He | 0.2 |
| *Ne | 0.1 |
| *Ar | 0.03 |
| Kr | 0.02 |
| Xe | 0.005 |
| *$N_2(A^3 \Sigma)$ | 0.001 |
| *$CO(a^3 \Pi)$ | $6 \times 10^{-5}$ |

The TOF spectrum for the helium, neon and argon beams as observed with the particle multiplier revealed only two peaks. The first is identified as the detection of resonant photons from the course discharge and the second as the detection of the respective metastable species of the source gas. The photon peak is established by the fact that this shape matches the aperture function, as it must for photons, and by the fact that the position of the peak in time with respect to the chopper wheel reference signal and the shape of the peak remain unchanged for multiplier displacements. The velocity of the slower peak is established equally by its separation in time from the photon peak and from its displacement in time resulting from a spatial displacement of the multiplier.

The most probable velocity and velocity distribution of the metastable species were obtained by assuming a weighted Gaussian for the distribution. It was determined by numerical integration that, for these measurements, the detector current was well approximated by the ideal case in which the chopper

wheel aperture was open for a time negligible compared to the time of flight. In this ideal case the velocity distribution, $f(v)$, is proportional to the time-of-flight spectrum, $I(t)$, multiplied by $t^2$, where vt is the detector-to-chopper wheel separation. The most probable velocities of the calculated distribution for the three metastable species were $1.8 \times 10^3 ms^{-1}$, $8.3 \times 10^2 ms^{-1}$ and $6.0 \times 10^2 ms^{-1}$ for helium, neon and argon, respectively, for source conditions of 3 mA discharge current and optimum nozzle pressures. These velocities correspond to energies of 66 meV, 72 meV and 74 meV, respectively. The half-widths of the velocity distributions were 45% for helium and 27% for neon and argon.

The specially designed metastable detector incorporates the principal features of a gas cell used by Dunning and Smith (6) to measure secondary emission coefficients. With this detector absolute flux measurements of the metastable component of the beam were obtained. The sensitive surface was a disc of chemically cleaned stainless steel or copper from which secondary electrons ejected by the beam were measured. The secondary electron ejection coefficients for the target surface for the three metastable species lie very close to unity (6). The flux at 3 mA emission and optimum pressure for the helium, neon and argon metastables was $3.5 \times 10^{14}$, $1.5 \times 10^{14}$, and $7.2 \times 10^{13}$ atoms $s^{-1}$ $sr^{-1}$, respectively. The flux values obtained for the different target surfaces agreed within the coefficient uncertainty. The photon flux was shown to contribute much less than 1% of the total secondary current.

## 5. $N_2{}^M$ Beam Source

The $N_2$ beam source design is identical to that of the rare-gas metastable source design. The source is essentially a glow discharge maintained in pure $N_2$ gas undergoing nozzle expansion. The expansion is across a 0.015 cm hole supporting a 50 Torr pressure gradient.

11

## 6. Metastable Quenching Rates - Penning Ionization

We had earlier measured the quenching rates of the metastable rare gas atoms He, Ne, Ar, and Kr with Cd and Zn (7,8). This work was originally motivated by the $He^M$ + Cd, Zn Penning process which we verified to be responsible for the inversion mechanism in the respective laser systems.

The $He^M$ + Cd, Zn Penning cross sections were also measured in our beam apparatus. This method has the advantage that the ions formed in the Penning ionization collision are counted directly and can be correlated directly with the $He^M$ loss rate.

The metastable beam entered a reaction volume after passing through a differential pumping wall. The background pressure in the reaction volume was between $10^{-7}$ and $10^{-6}$ Torr for all measurements. The oven containing the target material was supported in the center of the reaction volume. A schematic of the target oven is shown in Figure 2.

When Penning ions were formed along the beam path in the chamber, the uniform electric field set up by the bias plate voltage causes a given ion to move to the collection plate beneath it. All plates were kept near ground potential. The guard plates were permanently grounded to the chamber wall and served to eliminate the end effects of the electric field and target number density. The two large ion collection plates were separately supported from the end flange to eliminate possible leakage paths between them. The beam path was chosen to be closer to the bias plate in order that possible photoelectron ejection from the collection plates be made less likely.

The principal advantage of using two adjacent ion collection plates is that the measurement of the currents $I_1$ and $I_2$ at a single number density is sufficient to determine a value of the cross section. It is easy to show that the current ratio determines a cross section through the relation

$$\ell n(R) = QNX, \tag{1}$$

12

where R is the ratio $I_1/I_2$, Q is the total ionization cross section, N is the target number density, and X is the common length of the collection plates. In the measurements reported here, the current ratio was measured at several number density values to check for consistent cross-section values. By using this ratio method instead of the attenuation method, variations in the incident beam flux during the time the oven is changing temperatures are cancelled out and, further, the photon content of the transmitted beam need not be known.

The cadmium measurements were taken over the range from T = 205°C, where N = 8.9 x $10^{12}$ cm$^{-3}$, to T = 283°C, where N = 5.1 x $10^{13}$ cm$^{-3}$, where T is the oven temperature and N is the target number density.

The Cd data are shown in Figure 3 where the solid dots are the data points. The solid line represents the dependence of R on number density found by using Eq. (1) with Q equal to the best-fit cross section. The best-fit cross section is 10.6 x $10^{-15}$ cm$^2$. Previous pulsed afterglow measurements have yielded values of 4.5 x $10^{-15}$.
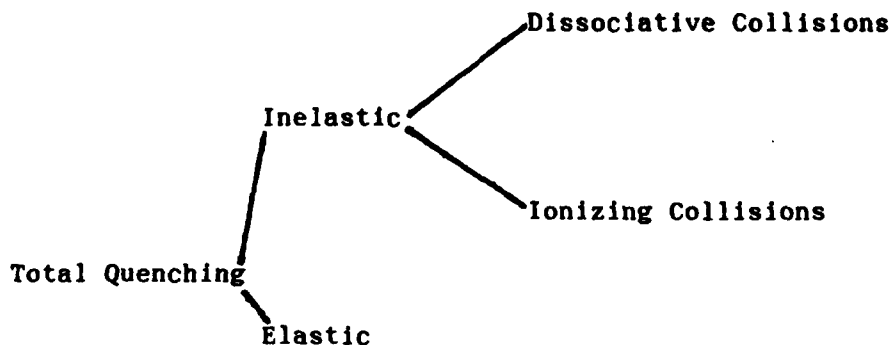
The zinc measurements were taken over the range from T = 297°C, where N = 2.2 x $10^{13}$ cm$^{-3}$, to T = 347°C, where N = 1.17 x $10^{14}$ cm$^{-3}$.

The zinc data are shown in Figure 4 where the solid dots are the data points and the solid line is determined by the best-fit cross section. The best-fit cross section is 3.5 x $10^{-15}$ cm$^2$. Previous pulsed afterglow measurements have yielded values of 2.9 x $10^{-15}$.

These results were correlated with both transmission loss measurements on the He$^M$ beam and optical observations of the emission from excited Penning ions.

## 7. Metastable Loss Rates/Total Quenching

The metastable interactions in the cell can be divided into several discrete processes, all of which scatter metastable atoms out of the beam:

```
                                        ,Dissociative Collisions
                                       /
                            Inelastic<
                           /           \
                          /             `Ionizing Collisions
                         /
        Total Quenching
                         \
                          `Elastic
```

In order to observe simultaneously all possible processes occurring in the reaction, a multi-electrode cell was constructed. This apparatus for the total metastable loss measurements is shown schematically in fig. 5 and the multi-cell is shown in fig. 6. The metastable beam density at the entrance to the cell is monitored by electrode #2 which is a grid of 10% transparency. As the metastable atoms traverse the cell and interact with the target species in the cell, the electrodes with appropriate bias voltages monitor the various processes occurring in the cell. A Baratron Gauge measures absolute pressures of gases in the cell while the pressure of condensable species is determined from vapor pressure curves and the cell temperature. The cell shown is capable of determining in a single set of measurements, Penning cross sections, total quenching rates, and elastic cross sections.

The cell was tested He metastable atoms incident on target gases of He, Ar, Kr, and $N_2$. Of the former target species the only inelastic process occurring is Penning ionization while the use of He as the target yields only elastic scattering processes.

In order to determine the cross sections for these reactions, we need to know the surface detection efficiency and the gas pressure. Using the surface

detection efficiencies determined by Dunning et al.(6), we are able to obtain

inelastic and elastic cross sections.  Typical data is shown in figs. 7-10.

Agreement with earlier results is excellent.  The results from this experiment

are shown along with other results in Tables 5 and 6.

## TABLE 5

### TOTAL QUENCHING CROSS SECTIONS ($cm^2$)

| Beam Species | $N^2$(M) | Ar(M) | He(M) |
|---|---|---|---|
| Target Species | | | |
| $N_2$ | | | $2.9x10^{-15}$ |
| $HgBr_2$ | $2.7x10^{-15}$ | $5.2x10^{-15}$ | $4.0x10^{-15}$ |
| $HgI_2$ | $3x10^{-15}$* | | |
| $HgCl_2$ | $2x10^{-15}$* | | |
| Cd | | $6.5x10^{-15}$^ | $4.5x10^{-15}$^ $10.6x10^{-15}$+ |
| Zn | | $5.3x10^{-15}$^ | $2.9x10^{-15}$^ $3.5x10^{-15}$+ |
| Ar | | | $2.2x10^{-15}$ $2.6x10^{-15}$ |
| Kr | | | $2.4x10^{-15}$ $7.8x10^{-15}$ |

* estimated from flowing afterglow observations
^ from pulsed afterglow ref (7)
+ from beam ref (8)

## TABLE 6

### ELASTIC CROSS SECTIONS ($cm^2$)

| Beam Species | $N_2$(M) | Ar(M) | He(M) |
|---|---|---|---|
| Target Species | | | |
| $HgBr_2$ | $2.3x10^{-14}$ | $4.7x10^{-14}$ | $4.2x10^{-14}$ |
| Ar | | | $4.6x10^{-15}$ |
| Kr | | | $4.5x10^{-15}$ |

## 8. Elastic Scattering

A glass oven with small holes drilled in either end was used to confine and define the interaction region for the measurement of elastic scattering losses for $N_2$, He, and Ar metastable species on $HgBr_2$. The density of the $HgBr_2$ in the cell is determined by measuring the temperature of the cell using thermocouple probes attached to the cell with Torr Seal and calculating the vapor pressure from vapor pressure-temperature data in the literature (9).

The collection angle for the detector was 0.5 degrees. Thus, the number obtained for the cross section represents the total loss of metastable atoms/molecules from the 0.5 degree beam. The results are shown in Table 7. Fig. 11 shows data for the elastic scattering of $He^M$ by $HgBr_2$.

### TABLE 7

### QUENCHING CROSS-SECTIONS/ELASTIC

| Metastable Species | Velocity | Cross Section |
|---|---|---|
| Helium | $1.5 \times 10^5$ cm/s | $4.2 \times 10^{-14}$ cm$^2$ |
| Nitrogen | $5.8 \times 10^4$ cm/s | $2.3 \times 10^{-14}$ cm$^2$ |
| Argon | $4.3 \times 10^4$ cm/s | $4.7 \times 10^{-14}$ cm$^2$ |

Since the total loss out of the beam is substantially greater than inelastic processes, we interpret these results to be the elastic-scattering cross sections.

### 9. $N_2$ Metastable Beam Interactions with Mercury-Halogens

Since the energy of the $N_2$ metastable species in the $A^3\Sigma$ state is less than the ionization potential of the target molecules, the inelastic losses are due to dissociative processes. The interaction of $N_2M$ with $HgBr_2$ is accompanied by the emission of light. Figure 12 shown the relative fluorescence observed in the range 400-560 nm for a monochromator resolution of 1.6 nm. The spectrum continues to decline in intensity without structure to

near 350 nm. The spectrum shown is in qualitative agreement with the spectrum of sidelight fluorescence from a $HgBr_2$ laser discharge. The fluorescence is identified as the $B^2\Sigma - X^2\Sigma$ transition in HgBr by referring to studies by Wieland (10). Laser output has been observed near the intensity maximum at 501.8 nm.

From such a fluorescence yield, it is clear that $N_2(A)$ molecules can directly populate the upper laser level in HgBr by dissociative excitation of $HgBr_2$. Because of the small interaction volume and the low beam and target densities, the excitation here is under single-collision conditions and hence precludes a two-step process. With accurate line density measurements of the target vapor, we can determine an effective cross section for the total quenching of $N_2(A)$ molecules by the Mercury-halogens, $HgBr_2$, $HgCl_2$, and $HgI_2$.

In order to be able to specify the target line density, we investigated the properties of effusive sources.

## 10. Effusive Source

The characteristics of the effusive source for the metal-halogens have been examined theoretically and experimentally.

For an ideal aperture with cross section A, the rate of effusion per unit solid angle per unit time is given by

$$\frac{dE}{d\Omega\, dt} = \frac{nA\bar{v}\cos\theta}{4\pi} \tag{2}$$

where n is the number density inside the oven, $\bar{V}$ is the average speed of the particles inside the oven, and $\theta$ is measured off the perpendicular to the surface containing the aperture.

The total volume element is given by $r^2 d\Omega dr$, so that

$$\frac{dE}{dV} = \frac{dE}{r^2 d\Omega\, dr} = \frac{nA\bar{v}\cos\theta}{4\pi r^2 dr}\,\frac{dt}{dr} \tag{3}$$

17

where dE/dt is the density. Using the geometry shown, $\cos(\phi) = y_0/r$, and $r = \sqrt{y_0^2 + \ell^2}$ so that

$$n' = \frac{dE}{dV} = \frac{nA\bar{V}y_0\,dt}{4\pi(y_0^2 + \ell^2)^{3/2}dr}$$ (4)

Taking the velocity of the beam particles as $K\bar{V}$, proportional to $\bar{V}$, the mean velocity in the oven, then $dt = dr/k\bar{v}$ and

$$n' = \frac{nAy_0}{4\pi k(y_0^2 + \ell^2)^{3/2}}$$

$$(n'\ell') = \int_{\ell_0}^{\ell_1} n'\,d\ell = \int_{\ell_0}^{\ell_1} \frac{nAy_0\,d\ell}{4\pi k(y_0^2 + \ell^2)^{3/2}}$$

$$= \frac{nAy_0}{4\pi k}\left\{\frac{\ell_1}{y_0^2(y_0^2 + \ell_1^2)^{1/2}} - \frac{\ell_0}{y_0^2(y_0^2 + \ell_0^2)^{1/2}}\right\}$$ (5)

For a long slit $A = w\,dx$ where $w$ is the width of the slit and $dx$ is the length. The above expression is integrated over the slit length with varying limits of integration corresponding to the actual geometry of the cell. The approximation $\ell_1 > y_0$, $\ell_0 > y_0$, and $\ell_1 \approx -\ell_0$ to obtain:

$$(n'\ell') = \frac{nA_s y_0}{4\pi k}\left\{\frac{1}{y_0^2} - \frac{-1}{y_0^2}\right\} \approx \frac{nA_s}{2\pi k y_0}$$ (6)

A further approximation uses K as $\approx 1$, to get

$$(n'\ell') = \frac{nA_s}{2\pi y_0}$$ (7)

where $A_s$ is the area of the slit width by length.

These characteristics for an ideal aperture have been compared with the experimental results obtained from closed cell measurements.

## 11. Total Quenching Cross Section Measurements

With a knowledge of the target line density, attenuation measurements of the metastable beam as it traverses the effusive source yields the total cross section for the scattering of the metastable particles by the target species:

$$I = I(0) \, Exp(-\sigma N l) \qquad\qquad (8)$$

or $\quad \ln(I/I(0)) = -\sigma N l$ $\qquad\qquad\qquad$ (9)

where $\quad$ I is the attenuated transmission intensity

$\qquad$ I(0) is the entrance beam intensity

$\qquad$ $\sigma$ is the scattering cross section

$\qquad$ N is the target density in $cm^{-3}$

and $\qquad$ l is the path length through the target in cm.

The cross section, $\sigma$, is the total scattering cross section and includes the quenching of the metastable species by the target and elastic scattering of the metastable particles out of the detected beam.

One can separate the total quenching and the elastic processes by making use of the fact that the elastic scattering, while in general having a larger cross-section than the quenching mechanism, is confined primarily to the forward direction within a rather small solid angle around the forward direction. Thus, if the detector subtends a large solid angle (defined by the limiting aperture at the detector and the distance to effusive source), elastic processes make a negligible contribution to losses out of the beam. If, on the other hand, the solid angle subtended is small (see, for example, the earlier section on elastic cross-section measurements), the major loss from the beam is due to elastic scattering.

For the quenching measurements our observation angle is approximately 18 degrees (compared to the 0.5 degrees for our elastic measurements). The line density in eq. (8) is determined in either of three ways:

19

1.  Reducing the detector observation angle to 0.5 degrees
    and using the elastic cross section measured earlier to
    obtain the line density,

2.  Calibrate the line density in terms of a known inelastic
    cross section,

3.  Use the calculated line density obtained from the
    hydrodynamic equations of effusive sources and vapor
    pressure data.

A typical metastable beam transmission signal versus the density inside

the effusive source (N.B. this is not the target line density) is shown in fig.

(13). The cross section is then obtained by using one or more of the

calibration methods described above to obtain the target line density. In

principle, method 3 above was the easiest to use since it requires only that we

measure the effusive source temperature. In practice, however, it is the least

reliable of the three methods and it gave us consistently cross sections that

were 3x larger than obtained with methods 1 and 2. Consequently, the results

reported in Table 5 for the total quenching of He and $N_2(A)$ metastable

particles by $HgBr_2$ used line densities calculated from the effusive source

properties but with a correction applied as determined from methods 1 and 2.

Methods 1 and 2 yielded internally consistent results.

The results for the quenching of $N_2(A)$ metastable molecules by $HgBr_2$ were

also checked by monitoring the HgBr emission as a function of the target

density as shown in fig. (14). The fluorescence measurements yielded the same

cross section within experimental limits.

## II.  OPTICAL EXCITATION IN FLOWING AFTERGLOW

This part of the report is itself divided into 4 parts:

1.  A description of the fast-flowing afterglow and the
    detection apparatus,

2.  The measurement of fluorescence efficiencies in the
    dissociative excitation of $HgBr_2$, $HgI_2$, and $HgCl_2$
    by $N_2(A)$ metastable molecules,

3.  The use of excitation transfer from $N_2(A)$ metastable
    molecules to neutral levels of Na, Cd, Zn, and Mg in
    order to determine the vibrational temperature of the
    nitrogen molecular beam,

and  4.  The fluorescence of a variety of molecular species dis-
    sociatively excited by metastable species.

### 1.  The Flowing Afterglow Apparatus

The fast flowing afterglow has proven to be a valuable laboratory tool in

the study of ion-atom and ion-molecule reaction rates (11), Penning ioniza-

tion (12), charge transfer (13), and chemiluminescence (14).  Its chief

advantage is that the observations are made in essentially a field-free region

in which the free electrons are thermalized.  Thus, the reactions of interest

can be studied without the competing effects produced by excitation and

ionization of atomic and molecular species by collisions with hot electrons.

The prinicpal observational tools used in flowing afterglow studies are the

mass spectrometer and optical emission from the excited afteglow products.  The

largest part of the work reported with the flowing afterglow has involved the

use of the noble gases, particularly helium, $N_2$, and other gaseous molecular

constituents.

In its simplest form the flowing afterglow consists of a long tube

connected at one end to a high-speed, high-capacity mechanical pump and the

other end terminated in a converging-diverging nozzle.  A carrier gas such as

helium is admitted at the entrance to the nozzle and flows downstream.  Flow

velocities are typically subsonic in the range $10^3 - 10^4$ cm $sec^{-1}$.  A weak

microwave discharge in the throat of the nozzle produces ions and metastable atoms with the neutrals of the carrier gas acting as a buffer inhibiting the diffusion of the ions and metastable atoms/molecules to the container walls. Downstream from the microwave discharge, provision is made to admit various impurity species which interact metastable atoms/molecules of the carrier gas.

Our flowing afterglow system is based on the design described by Schmeltekopf and Broida (15) with several minor modifications. The afterglow tube was fitted with a slide extension column which was terminated in a quartz window. The impurity port was replaced by a coaxial heater coil surrounding a small quartz vial containing impurity species. Under normal operating conditions the background helium pressure in the flow tube was less than 0.2 Torr and the flow velocity was $10^4$ cm sec$^{-1}$. Metastable densities approximately 25 cm downstream from the nozzle and at the location of the over are on the order of $10^{11}$ cm$^{-3}$.

The oven is heated to the point at which the metastable density was reduced by one-half. The mechanism presumably responsible for the quenching of the metastable atoms/molecules was dissociative excitation collisions with the vaporized impurity species. Quenching cross sections for helium triplet metastables in collisions with metal atoms are in the range $10^{-14} - 10^{-15}$ cm$^2$ (7). Consequently, we assume that the vapor densities for the experiments reported here are in the range $10^{12} - 10^{13}$ cm$^{-3}$.

The photon detection apparatus consists of a 1/4M Jarrel-Ash monochromator fitted with a 9783B photomultiplier. The output of the photomultiplier was sent to a single-channel analyzer and a multi-channel scaler. The monochromator wavelength and the MCS channel number were synchronously swept. Thus, the photon count at a particular wavelength is stored in one of the channels (1-2048) of the MCS. The MCS contents were subsequently stored on a microcomputer disc system for subsequent analysis and display.

The detection efficiency of the wavelength sensitive components is shown in fig. 15 for the spectral region between 200 and 650 nm. For absolute intensity measurements the system was calibrated against a tungsten-halogen standard lamp (18).

## 2. Fluorescence Efficiencies

Dissociative excitation of metal-bearing compounds by metastable species is frequently an efficient technique for producing atomic and molecular fluorescence. Such energy-transfer reactions yielding electronically excited products are of current interest as laser inversion mechanisms and in the lighting industry where emission from the metal (or intermediate compound) can be obtained more easily from the metal compound than directly from the lower vapor pressure metal.

The mercuric-halide compounds $HgBr_2$, $HgCl_2$, and $HgI_2$ have been of interest because of the laser output obtained on the $B^2\Sigma - X^2\Sigma$ transition in the Hg-halide radical (2). Dissociative excitation of the Hg-halide by the deactivation of $N_2(A^3\Sigma_u^+)$ has been shown to lead to population inversion on the $B^2\Sigma^+ - X^2\Sigma^+$ transition in HgBr and HgI (3-5). We report here the relative efficiencies for the generation of the B-X fluorescence following the dissociative excitation of $HgBr_2$, $HgI_2$ and $HgCl_2$ by $N_2 (A^3\Sigma_u^+)$:

$$N_2(A) + HgX_2 \ (X = Br, Cl, \text{ or } I) \rightarrow N_2(X) + HgX(B) + X, \qquad (10)$$

$$HgX(B) \rightarrow HgX(X) + h\nu. \qquad (11)$$
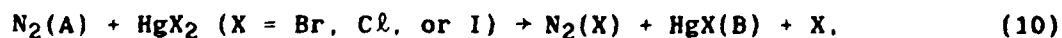
These reactions were studied with the flowing afterglow apparatus in use in our laboratory for many years (16). The flowing afterglow was modelled after that of Schmeltekopf and Broida (15) and the details are not repeated here.

The $N_2$ gas at the entrance to the flow system is expanded through a nozzle and excited with either a weak microwave discharge (< 2 watts) or a weak dc

discharge. The flow velocity is approximately $10^4$ cm s$^{-1}$ and the pressure in the reaction region 50 cm downstream from the source is $\sim 100\mu$. The near sonic velocity, low pressure, and weak excitation yield a source of $N_2(A)$ molecules with a vibrational population distribution characteristic of a temperature of 3200 - 4200° K which is representative of the vibrational temperature in an active discharge. Reactions of $N_2(A)$ with Cd, Zn, and Mg are used to determine the vibrational distributions (17). These reactions also permit us to assert that the source is uncontaminated by any other electronically excited species in the reaction region. The principal constituents of the afterglow are $N_2(X)$ molecules, $N_2$ ($A^3\Sigma$) metastable molecules, and $N(^4S)$ atoms. The estimated relative concentrations in the afterglow region which is approximately 50 cm from the active  wave discharge are $10^{16}$, $10^{12}$, $10^{13}$, cm$^{-3}$, respectively. The $N_2$ afterglow is a weak, nebulous blue color. Increasing the discharge power beyond 4 watts causes the afterglow color to assume the orange color characteristic of $N(^4S)$ recombination. At discharge powers below 4 watts the degree of molecular dissociation is relatively small.

We have observed the emission spectra in the region from 6500 - 3000A° resulting from the dissociative excitation of $HgX_2$ by $N_2(A^3\Sigma)$ molecules and determined the absolute relative photon yield for X = Cℓ, Br, and I.

The rate equation for the process

$$N_2 (A^3 \Sigma) + HgX_2 \rightarrow HgX (B^2 \Sigma) + X + N_2 \qquad (12)$$
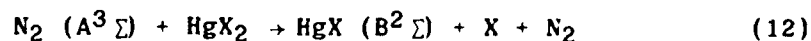
is given by

$$\frac{d}{dt} [HgX^*] = - \frac{[HgX^*]}{r} + k [N_2(A^3\Sigma)][HgX_2]. \qquad (13)$$

assuming that there is no collisional quenching of emitting states. $\tau_r$ is the

radiative lifetime of the emitting state, k is the rate constant for the formation of the HgX excited state, and the square brackets are the densities of the indicated state.

In steady-state

$$\frac{[HgX]}{R} = k \, [N_2(A^3 \,)][HgX_2] \qquad (14)$$

If the 3 species represented by X are observed under identical conditions:

$$I_{Cl} : I_{Br} : I_I = k_{Cl} : k_{Br} : k_I \qquad (15)$$

where I is the integrated photon flux.

Figure 16a shows the emission spectrum for $HgI_2$ in the region from 4800 – 3550 A°. The spectrum shown is uncorrected for variation in detector efficiency with wavelength. In order to obtain accurate relative intensity measurements, the detection system response was calibrated in the region of 300 – 700 nm by a quartz-iodine lamp referenced to NBS standards (18). Similar spectra are obtained for $HgCl_2$ and $HgBr_2$. The fluorescence is integrated over wavelength and we obtain

$$k_{Cl} : k_{Br} : k_I = 1.0 : 8.3 : 10.3. \qquad (16)$$

Since the formation of HgCl(B) by $N_2$(A, v=1) is endoergic by .05eV, emission from HgCl(B) must result from excitation by vibrationally excited $N_2$(A) molecules. At our measured vibrational temperature of 3200°K for the $N_2$(A) system, 13% of the $N_2$(A) population lies above the v=2 state. This accounts for the observed HgCl emission and the reduced but non-zero fluorescence efficiency relative to HgBr and HgI. It is unnecessary to invoke the presence of other electronically-excited, long-lived $N_2$ states to account for the HgCl emission.[4] The presence of any other energetic components in our

$N_2$ afterglow would be inconsistent with our observations involving energy transfer to Mg. Zn, and Cd. The results are summarized in Table 8. The absolute cross sections shown for the dissociative excitation to the fluorescing state are obtained by using the results of references 3 and 19.

TABLE 8

FLUORESCENCE CROSS SECTIONS ($cm^2$)

| Beam Species | $HgBr_2$ | $HgI_2$ | $HgCl_2$ |
|---|---|---|---|
| Target Species | | | |
| $N_2(M)$ Relative | 8.3 | 10.3 | 1.0 |
| $N_2(M)$-Absolute* | $.9x10^{-15}$ | $1.1x10^{-15}$ | $0.1x10^{-15}$ |

* Using $HgBr_2$ (fluorescence)/$HgBr_2$ total quenching from ref (3) and ref (19)

### 3. Determination of $N_2(A)$ Vibrational Distributions

#### (a) INTRODUCTION

Distributions of vibrational level populations of molecular states are of considerable interest. This interest has grown as the need for a better, more detailed understanding of the electrical properties of a gas discharge has progressed and as energy transfer from vibrationally excited molecules to other atomic or molecular systems is more and more utilized. In ion-molecule reactions, for example, vibrationally excited molecules can play a critical role in upper atmosphere chemistry (20).

Determining the vibrational distributions of radiating states is generally simple enough; one simply measures the relative intensities of the various vibrational transitions and combines it with the Franck-Condon factors to obtain the relative densities. The situation is more difficult in the case of non-radiating levels; e.g. the ground electronic state and/or metastable states

of the molecular system. In principle one can determine the densities of such non-radiating levels by using optical absorption. The difficulty here is that available optical sources are in general weak although a tunable laser may be used if one is fortunate enough.

A more generally useful method would be to somehow force the non-radiating levels to fluoresce. The equivalent process experimentally is to find a second species which will quench the vibrational state of interest and in a resonant energy transfer process cause the second species to be excited to a radiating level.

Here we describe the application of this method to the long-lived states of molecular nitrogen. Nitrogen is of great interest in atmospheric and plasma chemistry (21) and in laser plasmas (5,19). In particular the $N_2(A^3\Sigma)$ metastable state can be a very efficient system in which to store energy for subsequent transfer to other atomic and molecular systems (22).

Vibrational distributions were determined by Milne (23) by adding sodium vapor to a flowing nitrogen afterglow. Energy transfer collisions between vibrationally excited ground electronic levels of molecular nitrogen and sodium produced strong sodium excitation. This work suggested that the Na excitation temperatures corresponded to the vibrational temperatures of the ground $N_2(X^1\Sigma)$ state. Jolly et al (24) determined the vibrational level populations of $N_2(X^1\Sigma)$ in a pure nitrogen glow discharge by adding $He(2^3S_1)$ metastable atoms to the discharge. The reaction in this case is

$$He(2^3S_1) + N_2(X^1\Sigma,\nu) \rightarrow He(1^1S_0) + N_2^+(B^2\Sigma,\nu) + e. \qquad (17)$$
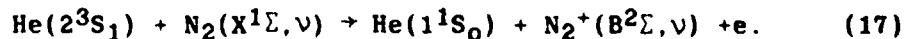
The fluorescent species in this case is the nitrogen molecular ion excited in the Penning collision between the metastable helium and the molecular nitrogen. Fahey et al (25) observed the excitation of cadmium and zinc to infer the vibrational distributions in a beam of $N_2(A^3\Sigma)$ metastable molecules

27

which were extracted from a cold cathode discharge; the vibrational temperature in this case being on the order of 4500 degrees kelvin.

We report here the use of energy transfer collisions between metastable molecular nitrogen and the atoms of Na, Mg, Cd, and Zn occurring in an afterglow of microwave-excited active nitrogen. The energy levels of Na are in near energy resonance with $N_2(X^1\Sigma,\nu)$ and permit one to determine the vibrational level populations of that system as in ref. (25). The excited states of the alkaline earths are in near resonance with the $N_2(A^3\Sigma,\nu)$ metastable state. Energy transfer from the $N_2(A)$ state to these species can thus be used to determine vibrational level populations in the $N_2(A)$ state as shown by Fahey et al. (25) who utilized Zn and Cd to obtain vibrational temperatures of the metastable nitrogen in a beam. The additional use of Mg extends the range over which useful vibrational temperatures may be obtained. The flowing active nitrogen afterglow has been used by several workers (23,4,26) to observe energy transfer from the active nitrogen species to the Hg-halides. In this case the fluorescence efficiencies of the HgX emission resulting from the energy transfer collision depends greatly on the vibrational populations of the $N_2(A^3\Sigma)$. There is thus interest in determining the effective vibrational temperature in this system.

### (b) EXPERIMENTAL APPARATUS

The flowing nitrogen afterglow apparatus is shown schematically in fig. 16. Molecular nitrogen is admitted at the entrance to the flow apparatus through a small expansion nozzle. The gas expands into a pyrex cross of 10 inch diameter. A weak microwave discharge is established in the nitrogen gas, localized by a quarter-wave, foreshortened cavity. The atom probe, consisting of a small oven which contains the atom of interest (Na, Cd, Zn, or Mg), is located approximately 50 cm downstream from the excitation region. In this region the short-lived discharge products have decayed and remaining in the

28

reaction zone are primarily N atoms and $N_2$ molecules both in their electronic groundstate, $N_2$ metastable molecules, and small concentrations of atomic and molecular ions which may be further reduced by electric field heating of the afterglow to increase the ambipolar diffusion rate.

The background $N_2$ pressure at the location of the atom probe is on the order of 0.1 Torr. The pressure in this region is kept low in order to minimize collisional effects in the excited states of the atom probe system. With the 540 cfm pump, consisting of a large mechanical forepump and a Roots blower exhausting the pyrex cross, the flow velocity is subsonic and on the order of $10^3$ to $10^4$ cm/s. The fluorescence produced by the interaction of the active nitrogen afterglow with the atom probe is observed at right angles to the flow direction through a quartz window by a 0.5m monochromator fitted with a photomultiplier. The detection system is operated in the photon counting mode with the pulses being counted and displayed by a multichannel scaler.

The weak nitrogen afterglow is a pale blue color. If the microwave excitation is increased above a nominal 1 watt, the afterglow assumes the characteristic orange glow associated with the recombination of atomic nitrogen. Since there is some evidence that the atomic nitrogen may quench the excited $N_2(A^3\Sigma)$ molecule, the system was generally operated at minimum excitation levels. With the addition of Na in the reaction zone a bright yellow flame appeared presumably resulting from transfer of energy from the vibrational system of the $N_2(X^1\Sigma)$ molecules to the electronic states of the Na. Magnesium produced a bright blue flame resulting from excitation by the $N_2(A^3\Sigma)$ system.

## (c) EXPERIMENTAL RESULTS & DISCUSSION

### (i) Energy Transfer Collisions

The excitation of the probe atom by the nitrogen is presumed to follow the reaction

$$\frac{dn_j^*}{dt} = -\frac{n_j^*}{\tau_j} + n_0 \sum_{\nu \geqslant \nu'}^{\infty} N_2(\nu)k(\nu) \qquad (18)$$

where the net rate of loss of excited state atoms from the probe source is

equated to the loss rate by photon decay and excitation by energy transfer

collisions between electronically and/or vibrationally excited molecular

nitrogen and the probe atom. $n_j^*$ is the excited probe atom density and $\tau_j$ is

the lifetime of the excited state. $n_0$ is the ground state probe atom density,

$N_2(\nu)$ is the population density of the vibrational level and $k(\nu)$ is the rate

constant. $N_2(\nu)$ is either the $N_2(X^1\Sigma)$ or $N_2(A^3\Sigma)$. The sum is carried out over

all those vibrational levels whose energy is sufficient to excite the

particular probe atom state. In general, except at high vibrational

temperatures, it is sufficient to use only the vibrational populations of the

level in closest energy coincidence with the

In steady state, we then have $n_j^*$.

$$\frac{n_j^*}{\tau_j} = n_0 \sum_{\nu \geqslant \nu'}^{\infty} N_2(\nu)k(\nu) \qquad (19)$$

$n_j^*/\tau_j$, however, is directly proportional to the intensity of the fluorescence

observed from the Na* state provided there are no collisional losses from this

state.

30

(ii)  Sodium Probe

The energy levels of atomic sodium are in near resonance with vibrationally excited $N_2(X^1\Sigma,\nu)$ molecules.  Thus, sodium may be used as the probe atom for this system as shown by Milne (23).  In fig. 17 we show the emission spectrum of Na from 600 to 400 nm.  Fluorescence from nD-3P states up to n=12 may easily be resolved.  In fig. 18 we plot the log of intensity, log (I), against the energy of the respective nD state.  In fig. 18 the intensities have been corrected for the spectral response of the instruments.

The plot of log (I) vs energy lies along an approximate straight line for n<9 (E<40000 $cm^{-1}$) suggesting that the vibrational populations of the $N_2(X^1\Sigma,\nu)$ system are in an equilibrium distribution.  If the cross-section for energy transfer is presumed not to vary significantly with vibrational level, we can infer the relative populations of the vibrational levels and obtain an equilibrium temperature of approximately 3100° k.  Milne (23) obtained temperatures near 4000° k in the Lewis-Raleigh afterglow region at pressures 50-100 times larger than those reported here.  The departure of the data from linearity for nD>8 is likely due to collisional ionization of the high lying Na states.  These states are within 0.2 eV of the ionization limit of sodium.

(iii)  Magnesium Probe

In fig. 19 is displayed the emission spectrum from 630 to 280 nm obtained when magnesium is used as the probe atom.  The energy levels of magnesium are in near resonance with vibrationally excited $N_2(A^3\Sigma)$ molecules.  A plot of the log of the intensity of the observed magnesium fluorescence lines terminating on the $3^3P$ level is shown in fig. 20.  Account has been taken of the differing statistical weights of the S and D levels.  The straight line drawn reflects a vibrational temperature of 3100° k, identical to the results obtained for the ground vibrational temperature.  This is to be expected since the hot electrons in the active microwave discharge provide the vibrational heating for both the

31

ground and metastable molecular systems.

There are several interesting features to be noted in the spectrum of fig. 19. The intercombination line at 457 nm ($3^3P_1$-$3^1S_0$) is relatively intense. However, emission from the nearby $3^1P_1$-$3^1S_0$ resonance line at 285 nm is not observable nor is any other emission line originating on a singlet level. In a typical magnesium discharge the intercombination line intensity is generally negligible compared to the intensity of the siglet resonance line. The absence of any significant population of the magnesium singlet levels suggests that there are strong selection rules governing the excitation transfer from the $N_2(A^3\Sigma)$ to the magnesium.

(iv) Cadmium Probe

In fig. 21 we show the fluorescence spectrum obtained when Cd is used as the probe atom. The energy levels of cadmium and zinc are energy resonant primarily with the higher vibrational levels of the metastable molecule. The transitions which appear in the spectrum are all from Cd levels which lie at or below the lowest vibrational state of the nitrogen; thus, in principle, all the vibrationally excited nitrogen is capable of energy transferring to the Cd. The results for Cd shown here are not useful for determining vibrational temperatures in the $3000^0$ k range. In reference (25) both Cd and Zn were used to infer vibrational temperatures above $4000^0$ k and the results here may be compared with that data.

Of perhaps more interest is again the apparent significance of spin selection rules in a molecular system. Energetically both the intercombination line in Cd and the resonance $5^1P_1$-$5^1S_0$ transition are capable of being excited by all the vibrational levels of the nitrogen. In a typical Cd discharge the resonance line is generally 2-3 orders of magnitude greater than the intercombination line. However, the energy transfer collisions do not populate

32

significantly any of the Cd singlet levels.

Also, we observe no emission from higher lying Cd triplet levels. If there are significant concentrations of other energetic, long-lived states of molecular nitrogen present in the afterglow as suggested by Dreilung and Setser (4), we would expect to see emission associated with energy transfer from these populations. No such anomolous fluorescence is observed in either Mg, Cd, or Zn spectra and we thus conclude that under the operating conditions described above, the metastable $N_2(A^3\Sigma)$ system is the only electronically excited species in the nitrogen afterglow.

### 4. Fluorescence due to Dissociative Excitation

The fast-flowing afterglow has proven to be a valuable laboratory tool in the study of ion-atom and ion-molecule reactions, Penning ionization, charge transfer, and chemi-luminescence. Its chief advantage is that the observations are made in essentially a field-free region in which the electrons are thermalized. Thus, the reactions of interest can be studied without the competing effects produced by excitation and ionization of atomic and molecular species by collisions with hot electrons.

The principal observational tools used in flowing afterglow studies are the mass spectrometer and the optical monochromator to analyze excited afterglow products. The largest part of the work reported with the flowing afterglow has involved the use of the noble gases, particularly helium, and molecules of atmospheric interest.

Our work with the flowing afterglow has been extended to interactions involving molecular metastable species such as $N_2(A)$ and molcular additives such as $HgX_2$ (X=halogen). In this section we compare chemi-luminescent reactions of the type:

$$He^M + PbI_2 \qquad \text{or}$$

$$N_2^M + PbI_2$$

with chemi-luminescence produced in reactions of the type:

$$He^M + Pb \qquad \text{or}$$

$$N_2^M + Pb$$
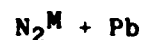
Figure 22-30b show, respectively

(1) Fluorescence spectrum from $He^M + Pb$.

(2) Fluorescence spectrum from $He^M + Bi$.

(3) Fluorescence spectrum from $He^M + Cd$.

In the above, the transitions labelled (I) are from neutral atoms; unlabelled lines are from transitions between ion levels. The above spectra are to be compared with:

(4) Fluorescence spectrum from $He^M + PbBr_2$.

(5) Fluorescence spectrum from $Ar^M + CdI_2$.

(6) Fluorescence spectrum from $N_2^M + CdBr_2$.

(7) Fluorescence spectrum from $He^M + SbI_3$.

(8) Fluorescence spectrum from $N_2^M + Cd$.

(9) Fluorescence spectrum from $He^M + SiH_4$.

One can draw some general conclusions from the observations:

(a) The interaction of the noble gas metastable atoms with atomic impurities yields typically ion fluorescence, presumably due to Penning ionization.

(b) Interaction of the metastable species with molecular ensembles results in dissociation of the molecule and yields principally emission from neutral species.

(c) The fluorescence spectra observed in (b) can be either molecular or

atomic in origin and presumably depends in detail on the relative energies of the systems and states involved. However, of more fundamental interest is the possible existence of selection rules in the dissociative excitation process.

The interaction of metastable helium atoms and metastable molecular nitrogen with $PbBr_2$, $GeI_4$, and $GaI_3$ were compared in the flowing afterglow system. Under comparable flow and titration rates optical emission in the visible region of the spectrum was observed only with He on $PbBr_2$. None of the other pairs showed any significant fluorescence. The figure shows a wavelength scan of the $He+PbBr_2$ interaction.

Only emission from the lowest lying resonance state of atomic Pb is apparent. Strong emission from lines at 4058A, 3683A, 3639A, and 2833A. These transitions originate from the $6S^2 6p7s$ excited triplet $P_{1}0_{0}$ state and terminate on the $6s^2 6p^2$ ground triplet $P_{2,1,o}$ level. Weak emission from other states is also seen.

We conclude that dissociative excitation of $PbBr_2$ by metastable helium has a large cross section. No additional quantitative observations can be made at this time.

In the following we investigate and compare dissociative excitation of $CdBr_2$ and $CdI_2$ by metastable He, Ar, and $N_2$. As an example of the fluorescence observations, we examine the interactions:

$$CdBr_2 + N_2^m \text{ and } CdI_2 + Ar^m$$
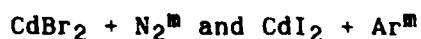
Table 9 lists the transitions observed. Figure 31 is a level diagram of Cadmium indicating the pertinent energy levels and transitions. Figures 32 and 33 show the actual fluorescence spectra obtained uncorrected for system response.

The $CdI_2:Ar^m$ fluorescence is virtually identical to the emission spectrum obtained from $CdBr_2:Ar^m$. For this system only atomic, neutral emission lines

from excited Cadmium are present. (The molecular structure near the 326.2 nm intercombination line in Cd is due to water vapor impurities present in the system). The background emission above 400.0 nm is blackbody radiation from the $CdI_2$ oven.

Emission from $CdBr_2:N_2^m$ shows a single Cd emission line at 326.2 nm (the intercombination line $5^3P_1 - 5^1S_0$). The line at 254.0 nm has not been identified. There also appears to be some molecular emission near 326.2 nm. Figure 33b expands the intensity scale of fig. 33a by an order of magnitude to bring out the molecular emission. This molecular feature does not appear in excitation with the metastable noble gas atoms and is unique to the $N_2$ excitation. This molecular emission has not been identified.

Table 10 contains similar information for excitation of $CdBr_2$ by $Ar^m$ and $He^m$.

It is interesting to note that the $Ar^m$ interaction generates considerably greater fluorescence than does the $He^m$. Presumably the ionization channel in $He^m + CdBr_2$ is much more efficient. We note also that emission from the $5^3D$ states in Cd is absent for $He^m$ – perhaps due to the fact that the helium metastable is a $^3S$ while the $Ar^m$ is a $^3P$. The $5^1P - 5^1S$ resonance transition is considerably weaker for both systems, reflecting the fact that both metastables are triplets. We thus suggest that in these dissociative reaction processes, selection rules on spin and orbital angular momentum are operative. This suggests that if the spin angular momentum in the metastable atom is oriented, it might be transferred to the dissociation products and observed. Figs. 34 and 35 show the spectra for $CdBr_2 + Ar^m$ and $CdBr_2 + He^m$.

## TABLE 9

| Observed Line | Transition | Reaction | Relative Intensity |
|---|---|---|---|
| 508.9 nm | $6^3S_1 - 5^3P_2$ | $CdI_2 + Ar^m$ | 85 |
| 479.9 nm | $6^3S_1 - 5^3P_1$ | $CdI_2 + Ar^m$ | 80 |
| 467.8 nm | $6^3S_1 - 5^3P_0$ | $CdI_2 + Ar^m$ | 50 |
| 361.0 nm | $5^3D - 5^3P_2$ | $CdI_2 + Ar^m$ | 30 |
| 346.4 nm | $5^3D - 5^3P_1$ | $CdI_2 + Ar^m$ | 20 |
| 340.3 nm | $5^3d - 5^3P_0$ | $CdI_2 + Ar^m$ | 7 |
| 326.2 nm | $5^3P_1 - 5^1S_0$ | $CdI_2 + Ar^m$ | 100 |
| 229.4(II) nm | $5^1P_1 - 5^1S_0$ | $CdI_2 + Ar^m$ | 6 |
| 254.0(II) nm | ? | $CdBr_2 + N_2^m$ | 25 |
| 326.2 nm | $5^3P_1 - 5^1S_0$ | $CdBr_2 + N_2^m$ | 100 |

## TABLE 10

Excitation of $CdBr_2$ by $Ar^m(4^3P_{2,0})$ and $He^m(2^3S_1)$

| Line (Angstrom) | Transition | Intensity ($He^m$) | Intensity ($Ar^m$) |
|---|---|---|---|
| 5085 | $6^3S_1 - 5^3P_2$ | 16 | 65 |
| 4799 | $6^3S_1 - 5^3P_1$ | 12 | 55 |
| 4678 | $6^3S_1 - 5^3P_0$ | 1 | 22 |
| 2294 II | | 2 | 16 |
| 3610 | $5^3D - 5^3P_2$ | - | 28 |
| 3464 | $5^3D - 5^3P_1$ | - | 12 |
| 3403 | $5^3D - 5^3P_0$ | - | 4 |
| 3262 | $5^3P_1 - 5^1S_0$ | 100 | 100 |
| 2295 II | $5^1P_1 - 5^1S_0$ | .1 | .1 |
| 4416 ($Cd^+$) | $5^2D_{5/2} - 5^2P_{3/2}$ | 2 | - |

# REFERENCES

1. T. P. Pan and R. M. Martin, J. Chem. Phys. **82**, 2226 (1978).

2. William L. Nighan, Appl. Phys. Lett. **36**, 1973 (1980).

3. R. S. F. Chang and R. Burnham, Appl. Phys. Lett. **36**, 397 (1980).

4. T. D. Dreiling and D. W. Setser, Chem. Phys. Lett. **74**, 211 (1980).

5. D. W. Fahey and L. D. Schearer, J. Chem. Phys. **72**, 6318 (1980).

6. F. B. Dunning and A. C. Smith, J. Phys. B **4**, 1696 (1971).

7. L. A. Riseberg, W. F. Parks, and L. D. Schearer, Phys. Rev. **8**, 1963 (1973).

8. D. W. Fahey, W. F. Parks, and L. D. Schearer, J. Chem. Phys. **72**, 2310 (1980).

9. HgBr$_2$ vapor pressure

10. K. Wieland, Helv. Phys. Acta **2**, 45, 77 (1929); **14**, 420 (1941); Z. Phys. **76**, 801 (1932); **77**, 157 (1932); Z. Elektrochem. **64**, 761 (1960).

11. F. C. Fehsenfeld, A. L. Schmeltekopf, P. D. Goldan, H. I. Schiff, and E. E. Ferguson, J. Chem. Phys. **44**, 4087 (1966).

12. R. C. Bolden, R. S. Hemsworth, M. J. Shaw, and N. D. Twiddy, J. Phys. B **3**, 61 (1970).

13. A. R. Turner-Smith, J. M. Green, and C. E. Webb, J. Phys. B **6**, 114 (1973).

14. T. S. Wauchop and H. P. Broida, J. Quant. Spectrosc. Radiat. Transfer, **12**, 371 (1972).

15. A. L. Schmeltekopf, Jr., and H. P. Broida, J. Chem. Phys. **39**, 1261 (1963).

16. L. D. Schearer, Phys. Rev. **A10**, 1380 (1974).

17. Submitted for publication.

18. R. Stair, W. E. Schneider and J. K. Jackson, Appl. Opt. **2**, 1151 (1963).

19. R. Burnham, Appl. Phys. Lett. **33**, 156 (1978).

20. E. C. Zipf, J. Chem. Phys. 47, 2034 (1963).

21. D. L. Albritton, "Energy Dependence of Ion-Neutral Reactions Studied in Drift Tubes", in Kinetics of Ion-Molecule Reactions, ed. by P. Ausloos (Plenum, New York, 1979), p119.

22. G. Cernogora, L. Hochard, M. Touzeau, and C. Matos Ferreira, J. Phys. B 14, 2977 (1981).

23.  E. L. Milne, J. Chem. Phys. 52, 5360 (1976).

24.  J. Jolly, M. Touzeau, A. Ricard, J. Phys. B 14, 2977 (1981).

25.  D. W. Fahey, W. F. Parks, and L. D. Schearer, J. Chem. Phys. 71, 2840
     (1979).

26.  L. D. Schearer, to be published, J. Chem. Phys. Jan. 1985.

## PUBLICATIONS/PRESENTATIONS

1. Presentation:  "Total Quenching Cross-Sections of Metastable Atoms and
   Molecules by $HgBr_2$", J. R. Daniels and L. D. Schearer, 35th Gaseous
   Electronics Conference.  Abstract published in Bull. Am. Phys. Soc. 28, 178
   (1983).

2. Presentation:  "Relative Fluorescence Efficiencies for Mercury Halide Vapors
   Excited by $N_2(A)$", L. D. Schearer, 35th Gaseous Electronics Conference.
   Abstract published in Bull. Am. Phys. Soc. 28, 178 (1983).

3. Presentation:  "Excitation of Mg, Cd, and Zn in a Flowing $N_2$ Afterglow", L.
   D. Schearer, DEAP (1983). Abstract published in Bull. Am. Phys. Soc. 28, 805
   (1983).

4. Presentation:  "Dissociative Excitation of Metal-Bearing Compounds by
   Metastable Atoms and Molecules", L. D. Schearer, Symposium on Atomic and
   Surface Physics, Feb 1984. Hintermoos, Austria. Article published in
   Proceedings SASP84, pp 341, 1984.

5.  "Relative Fluorescence Efficiencies for the Dissociative Excitation of Some
    Hg-Halides by $N_2(A^3\Sigma)$", L. D. Schearer, Jour. Chem. Phys., to be published
    Jan. 1985.

6.  "Energy Transfer Collisions between Vibrationally Excited Molecular
    Nitrogen and Mg, Cd, Zn, and Na", L. D. Schearer, submitted for
    publication.
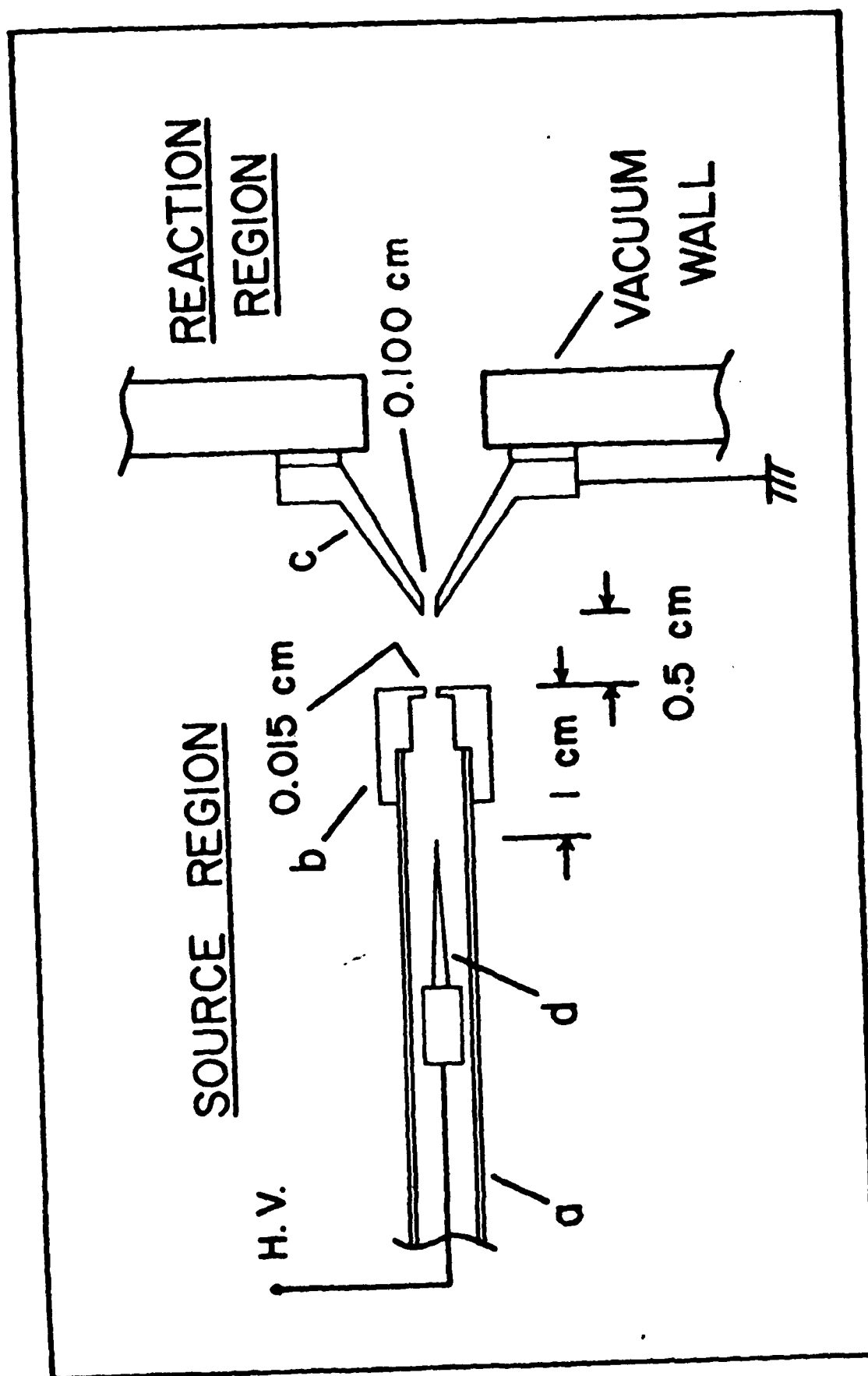
Figure 1. Nozzle source design showing Pyrex tube (A), boron nitride nozzle (B), skimmer (C), and needle or needle array (D).

41
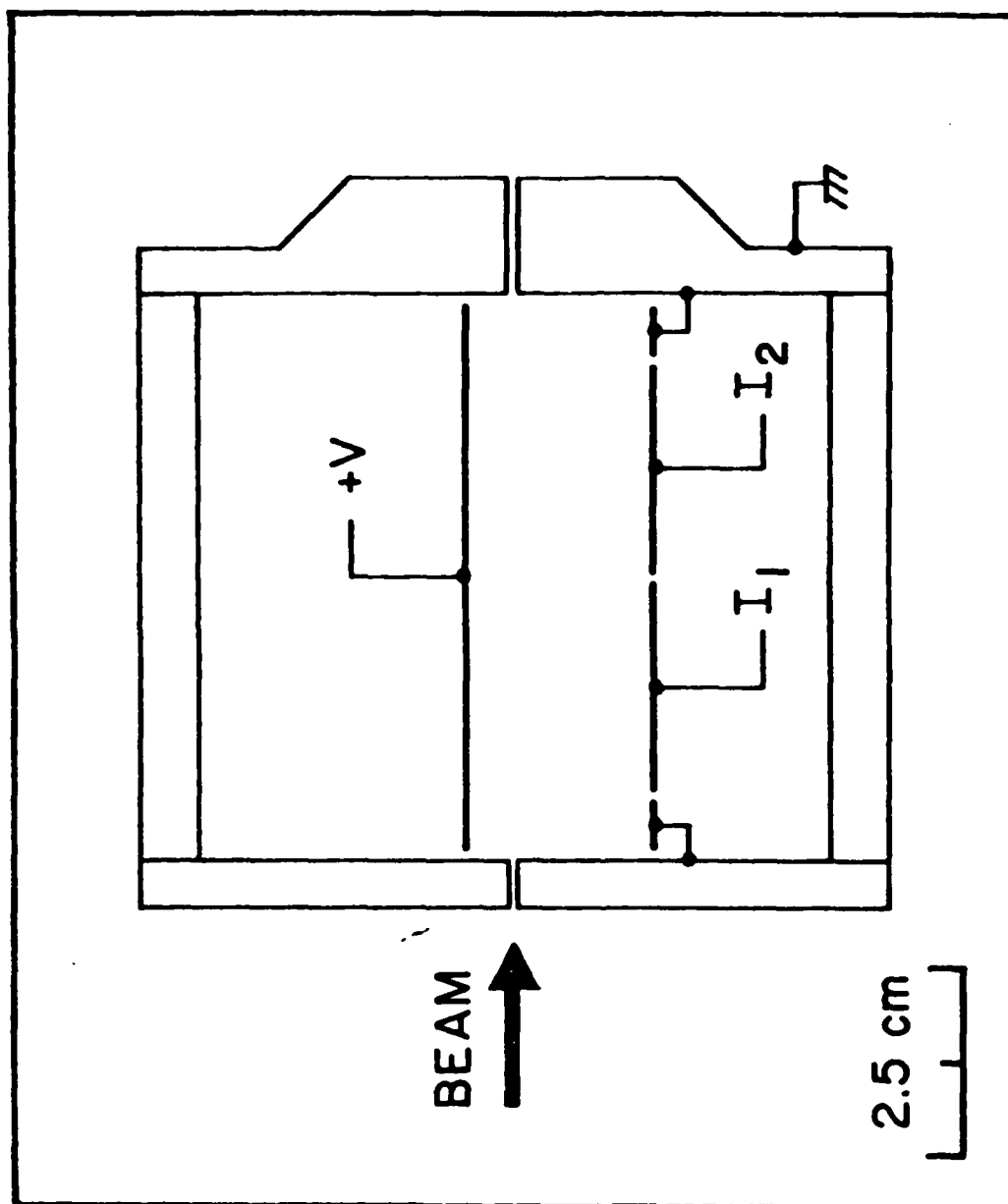
Figure 2. Schematic of reaction zone showing electrode placement to detect Penning ions.

42
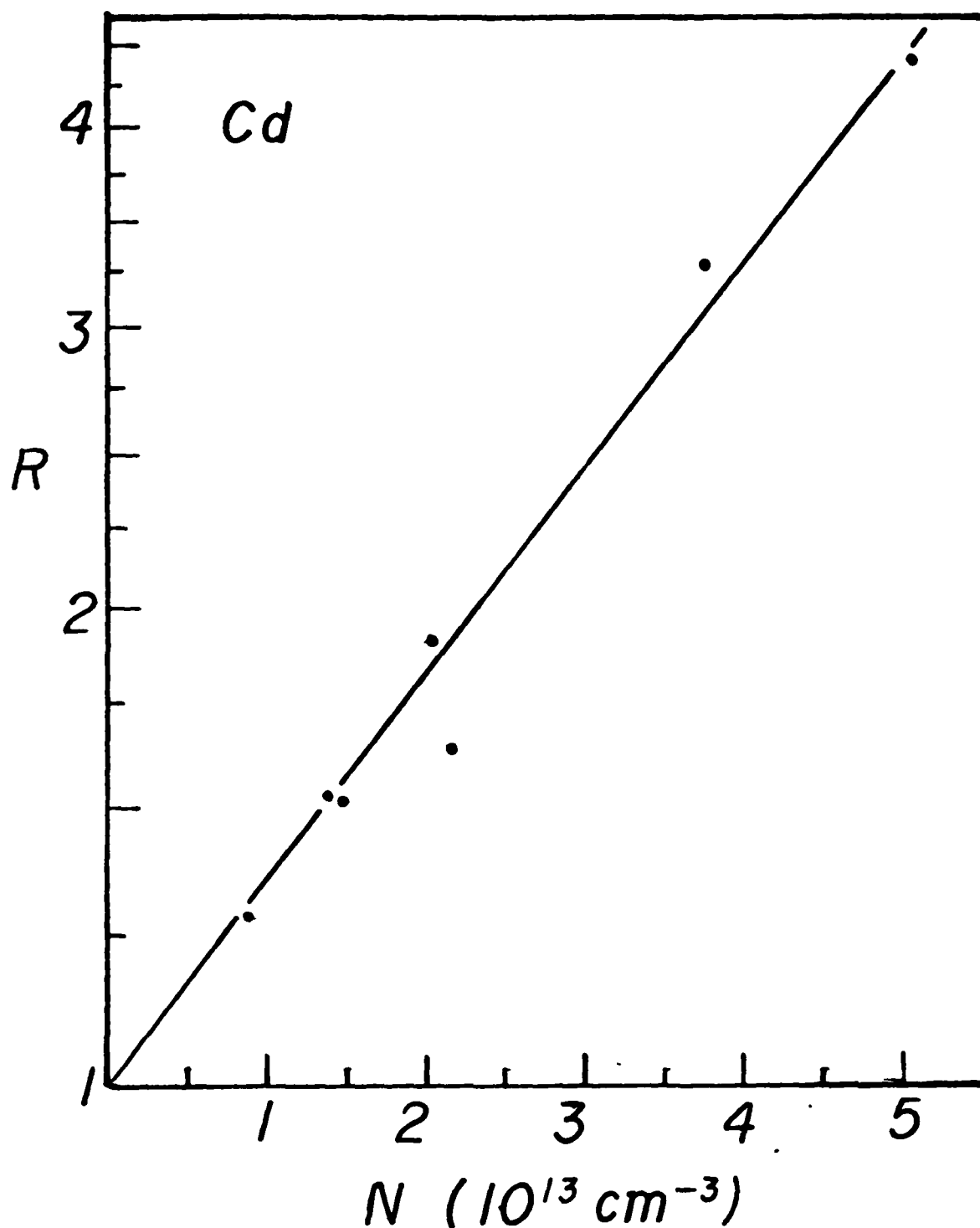
Figure 3.  Plot of R, the ratio of collection plate currents $I_1$ and $I_2$, vs.
number density for a Cd target.  The solid dots are the experimental points and the solid line is the R dependence for the
best-fit cross section of $10.6 \times 10^{-15}$ cm$^2$.
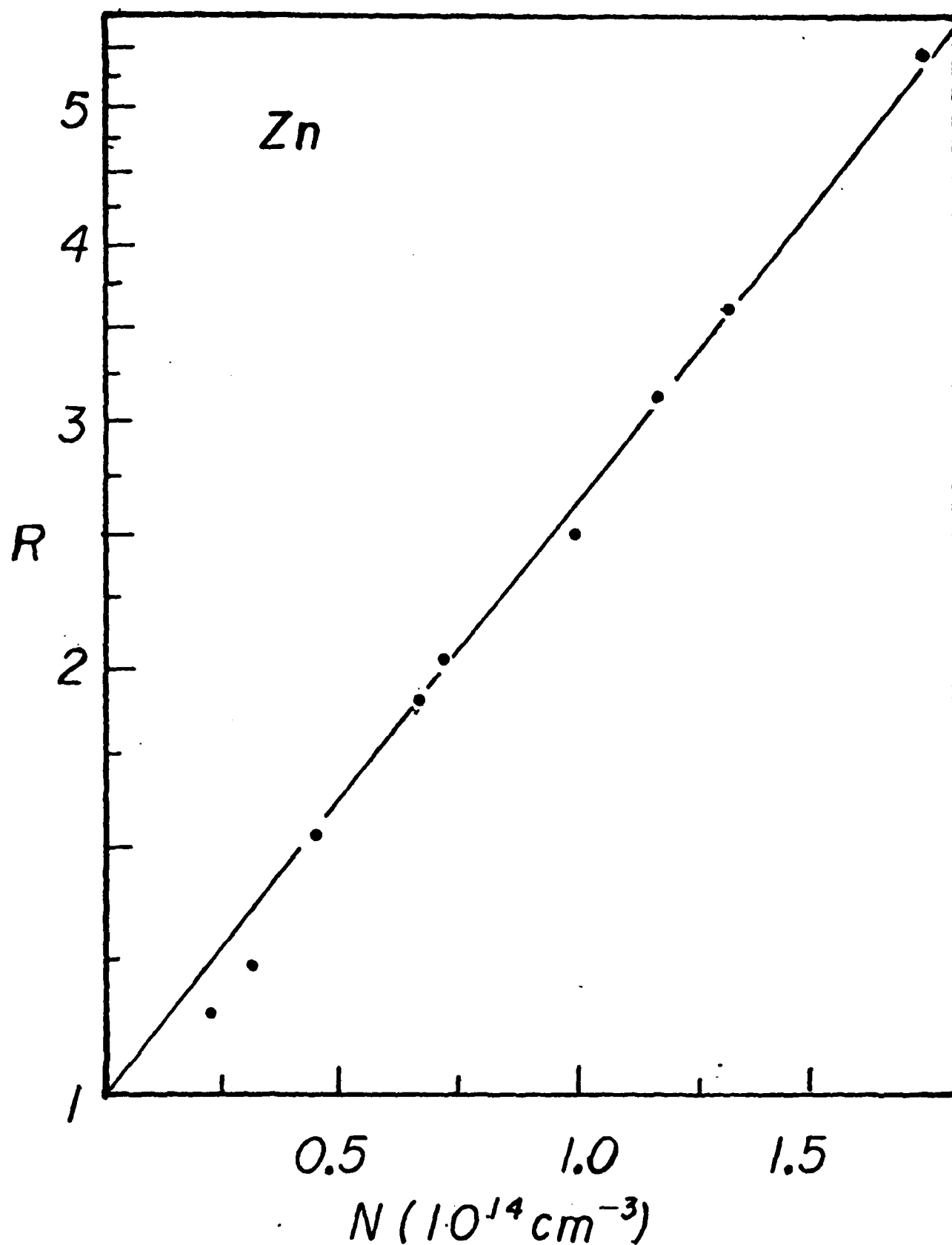
Figure 4. Plot of R, the ratio of collection plate currents $I_1$ and $I_2$, vs. number density for a Zn target. The solid dots are the experimental points and the solid line is the R dependence for the best-fit cross section of 3.5 x $10^{-15}$ cm².
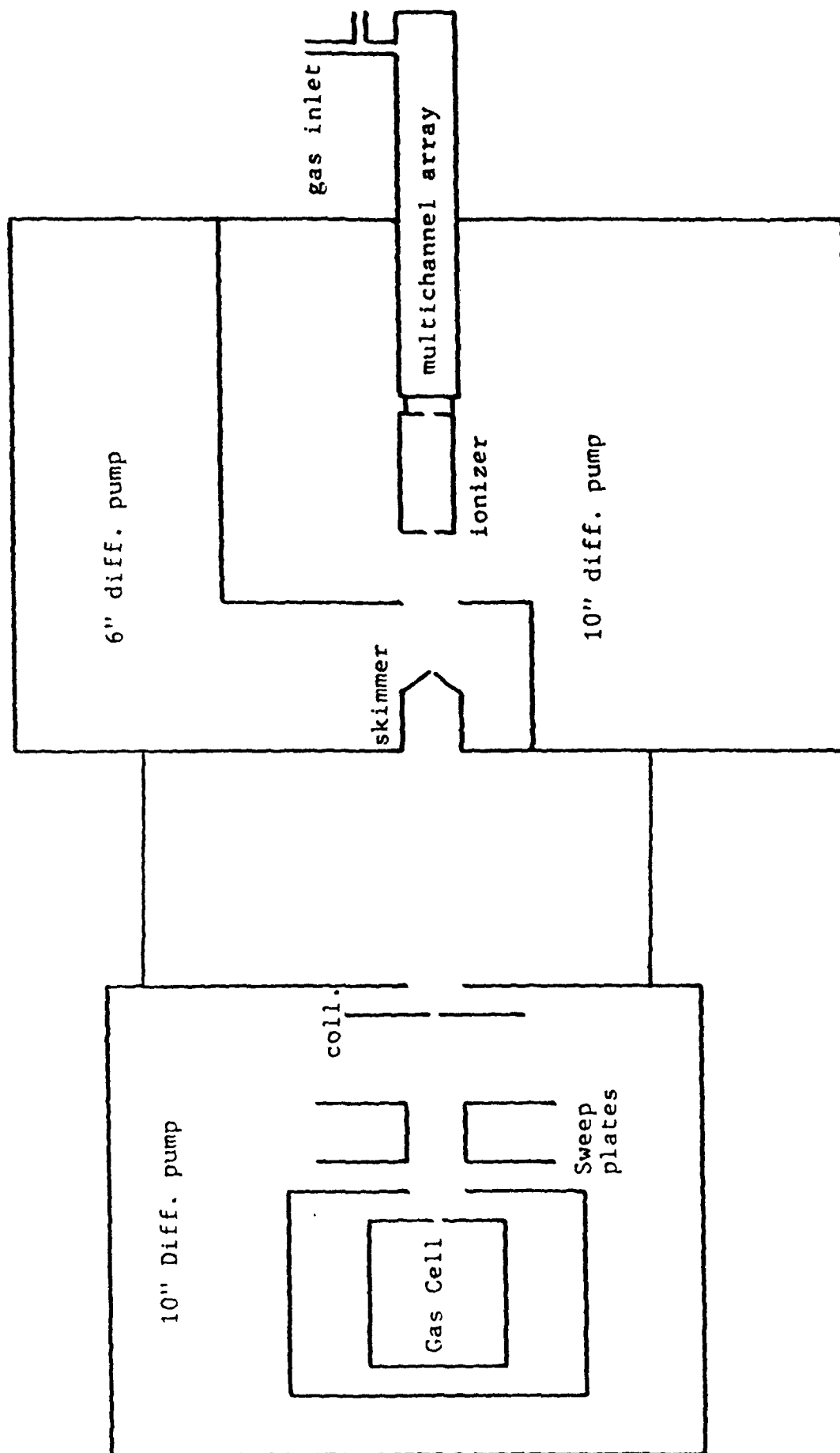
Figure 5.  Source and Scattering Chamber Assembly.  Schematic shows multi-channel array, ionizer, and skimmer/collimator assembly.  The box labelled "Gas Cell" is the assembly of fig. 6.  The multi-channel array eliminates the uv photon background but otherwise yields a weaker metastable flux.
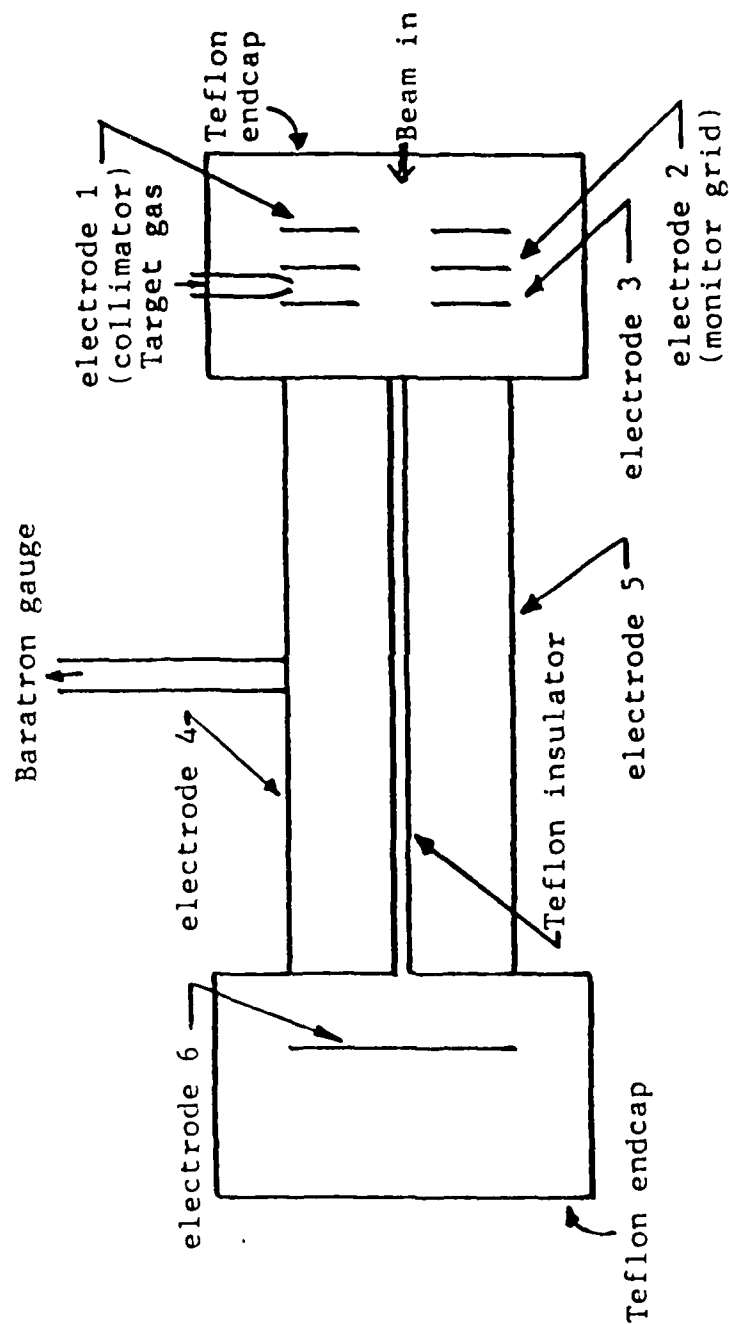
Figure 6. Schematic of multi-electrode cell. With appropriately biased electrodes the total quenching, elastic, and Penning processes could be observed with a single set of current measurements.
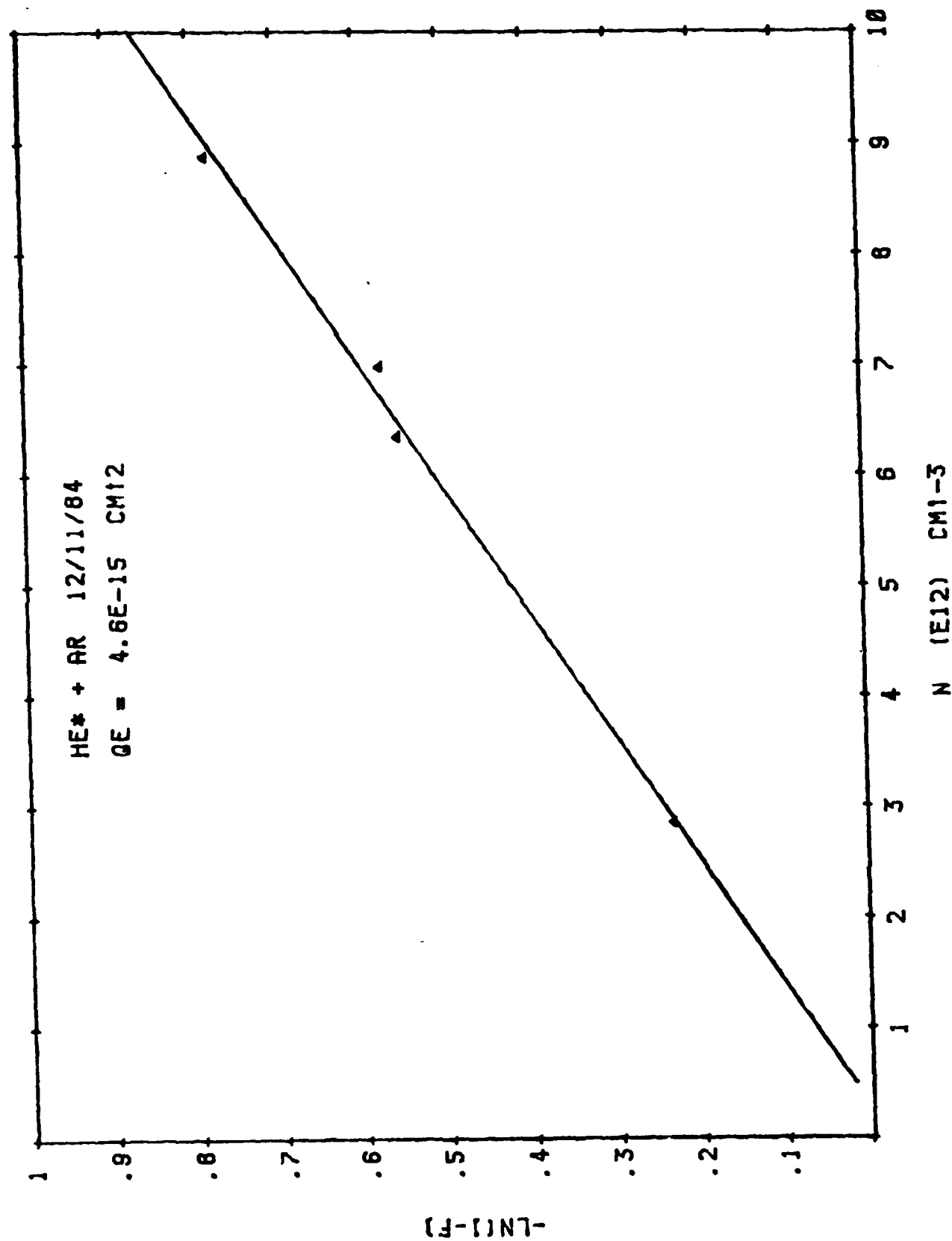
Figure 7. Elastic scattering $He^m$ = Ar. The natural log of current versus Ar density in cell.
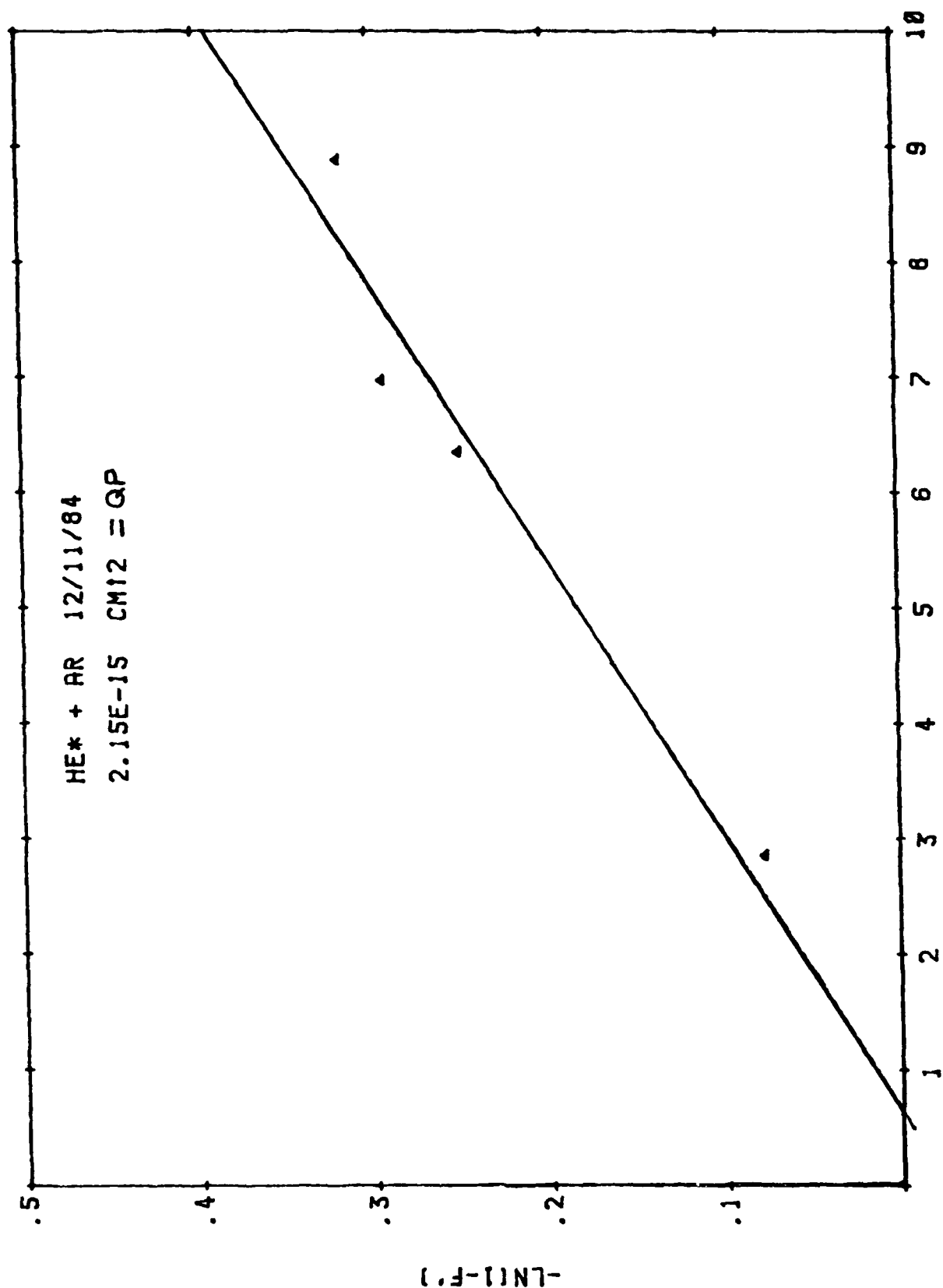
Figure 8. Penning cross-section $He^m + Ar$. The natural log of current vs Ar density in cell.
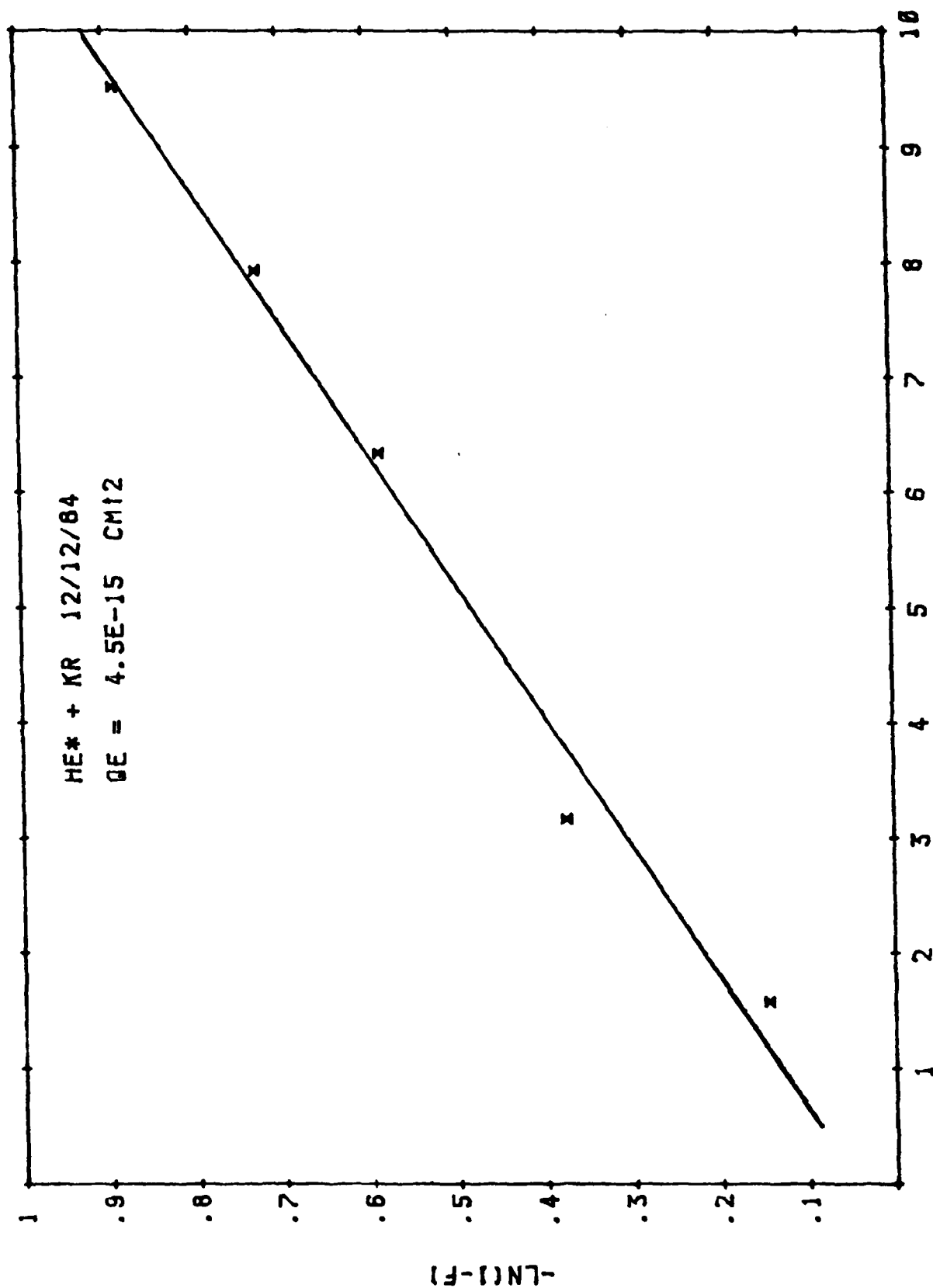
Figure 9. Elastic scattering He^m + Kr.

49
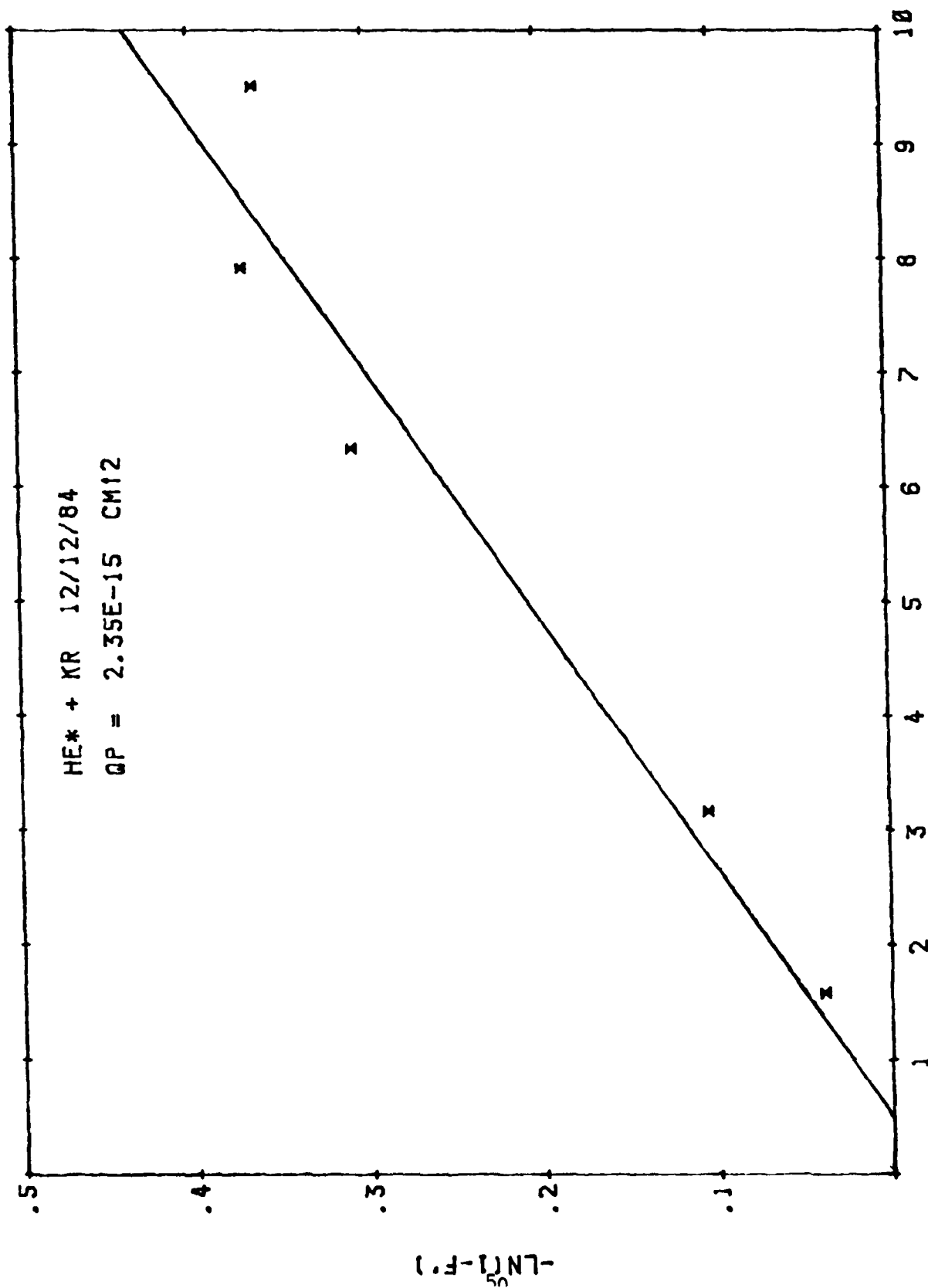
Figure 10. Penning cross-section $He^m$ + Kr.
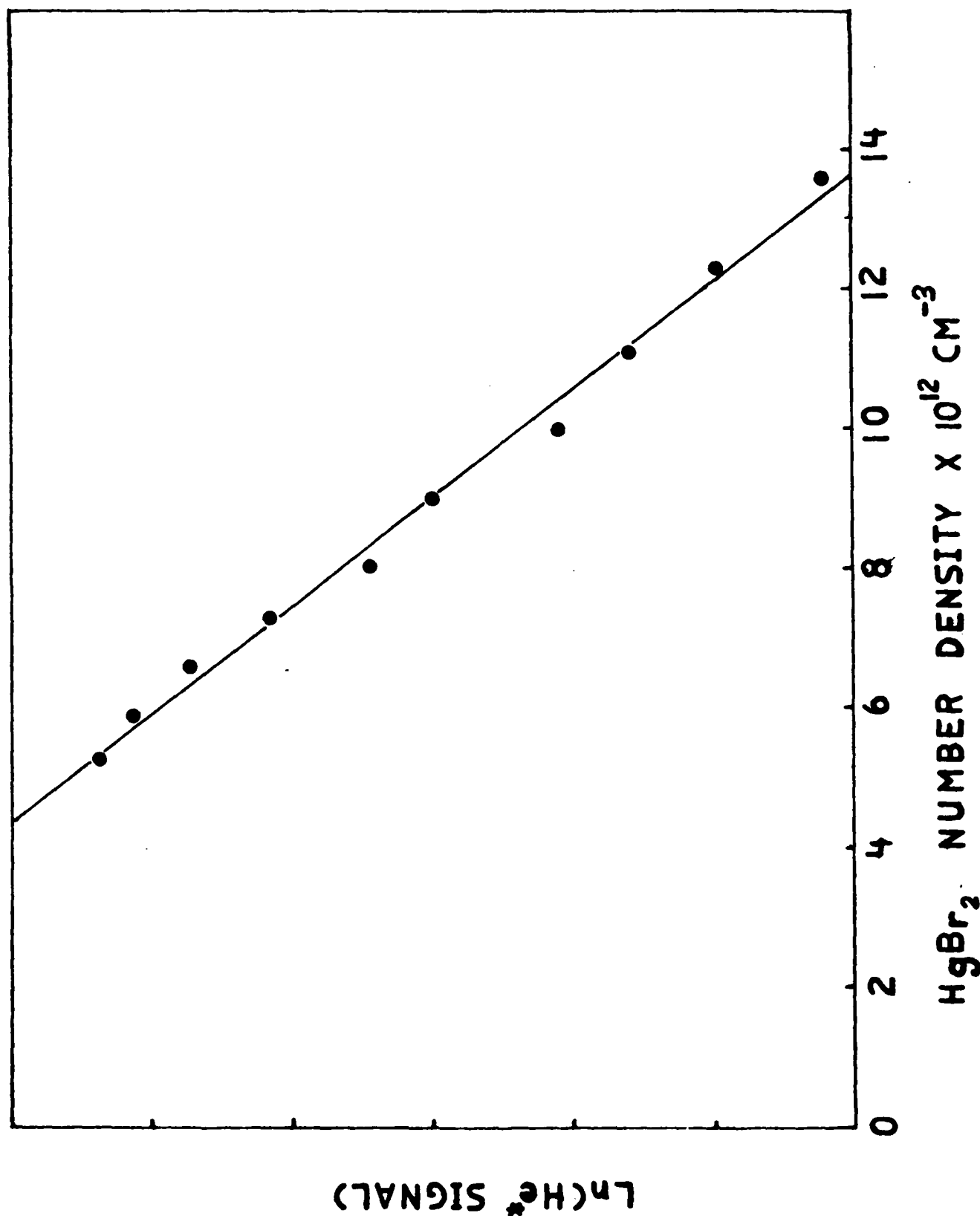
Figure 11. Attenuation of He$^m$ by HgBr$_2$ in cell with small entrance-exit apertures for observation of elastic scattering. Plot of natural log of helium transmission versus HgBr$_2$ density in cell.
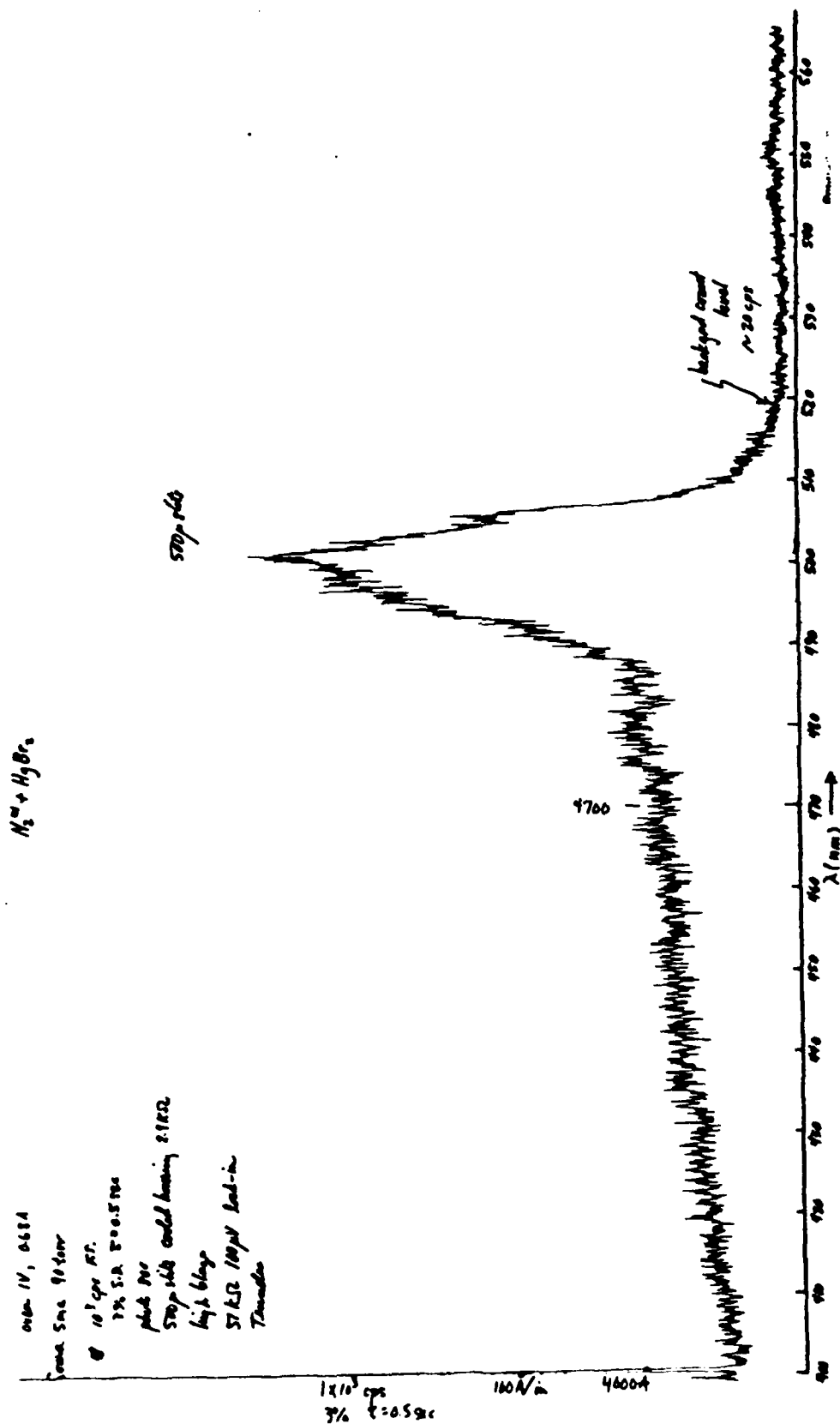
Figure 12. Plot of relative intensity vs. wavelength of the HgBr(B-X) fluorescence resulting from collisions of $N_2(A^3\Sigma_u^+)$ with $HgBr_2$. Monochromator resolution is 1.6 nm. Second order $Hg(6^3P)$ emission at 507.4 nm is also present in the spectrum as indicated.

52
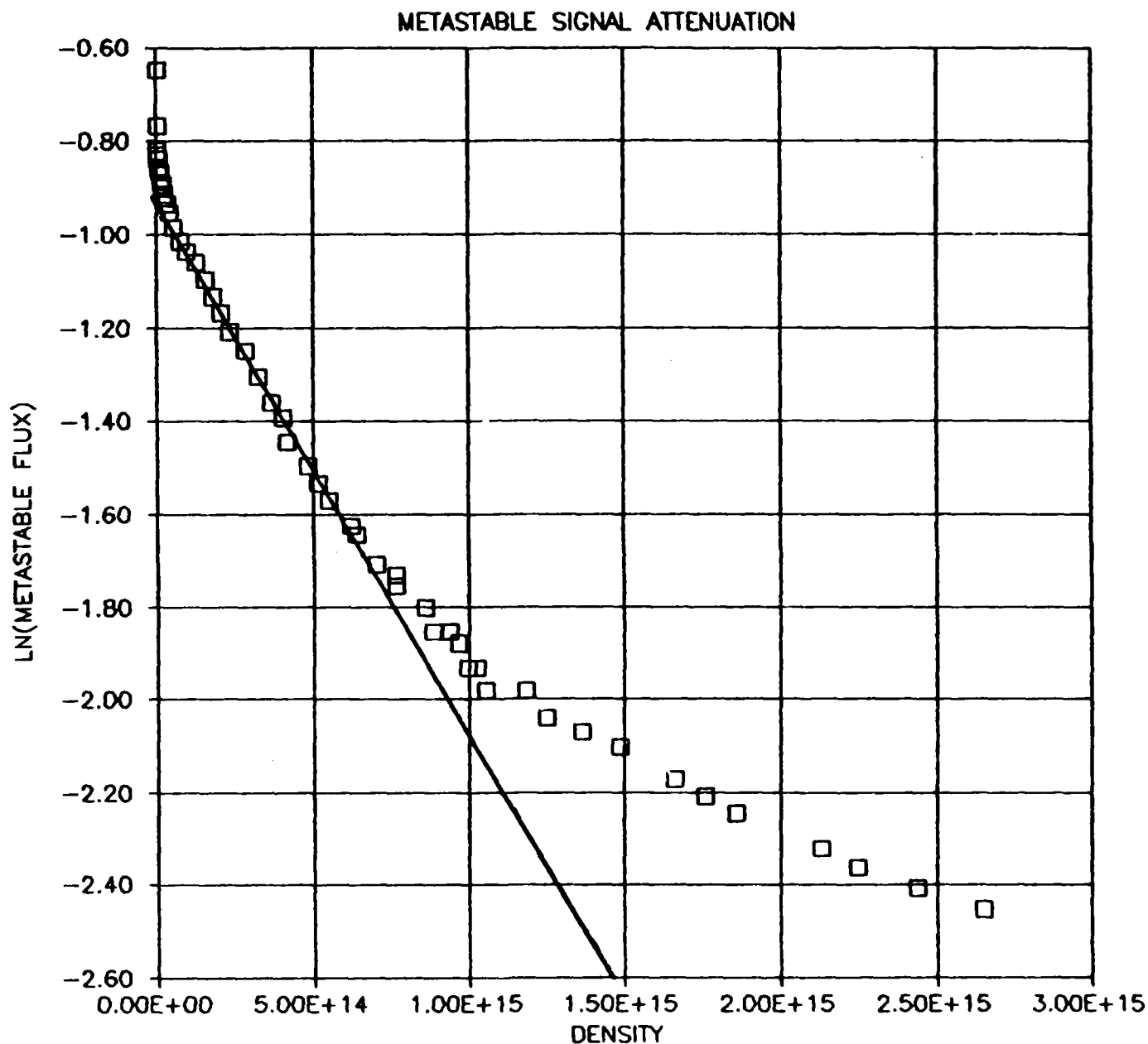
Figure 13. Transmission of $N_2$ metastable molecules through $HgBr_2$ effusive
source. Plot of natural log of $N_2^m$ molecules transmitted vs effusive
source density. The departure from linearity at high $HgBr_2$ densities
results from contamination of the particle detector by the $HgBr_2/Br_2$.
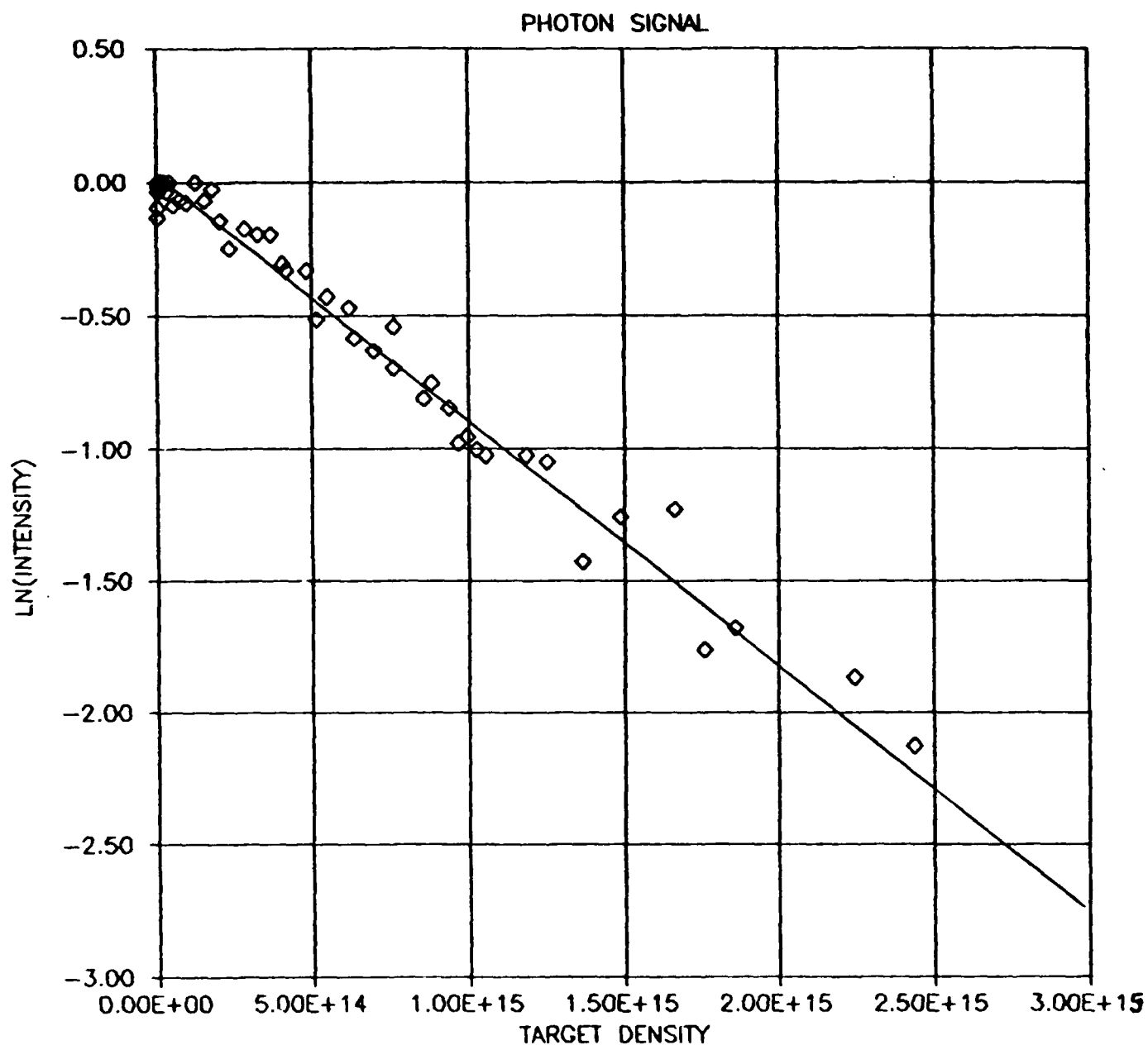
Figure 14. Plot of photons from HgBr decay as a function of $HgBr_2$ effusive source density. $N_2^m + HgBr_2$.
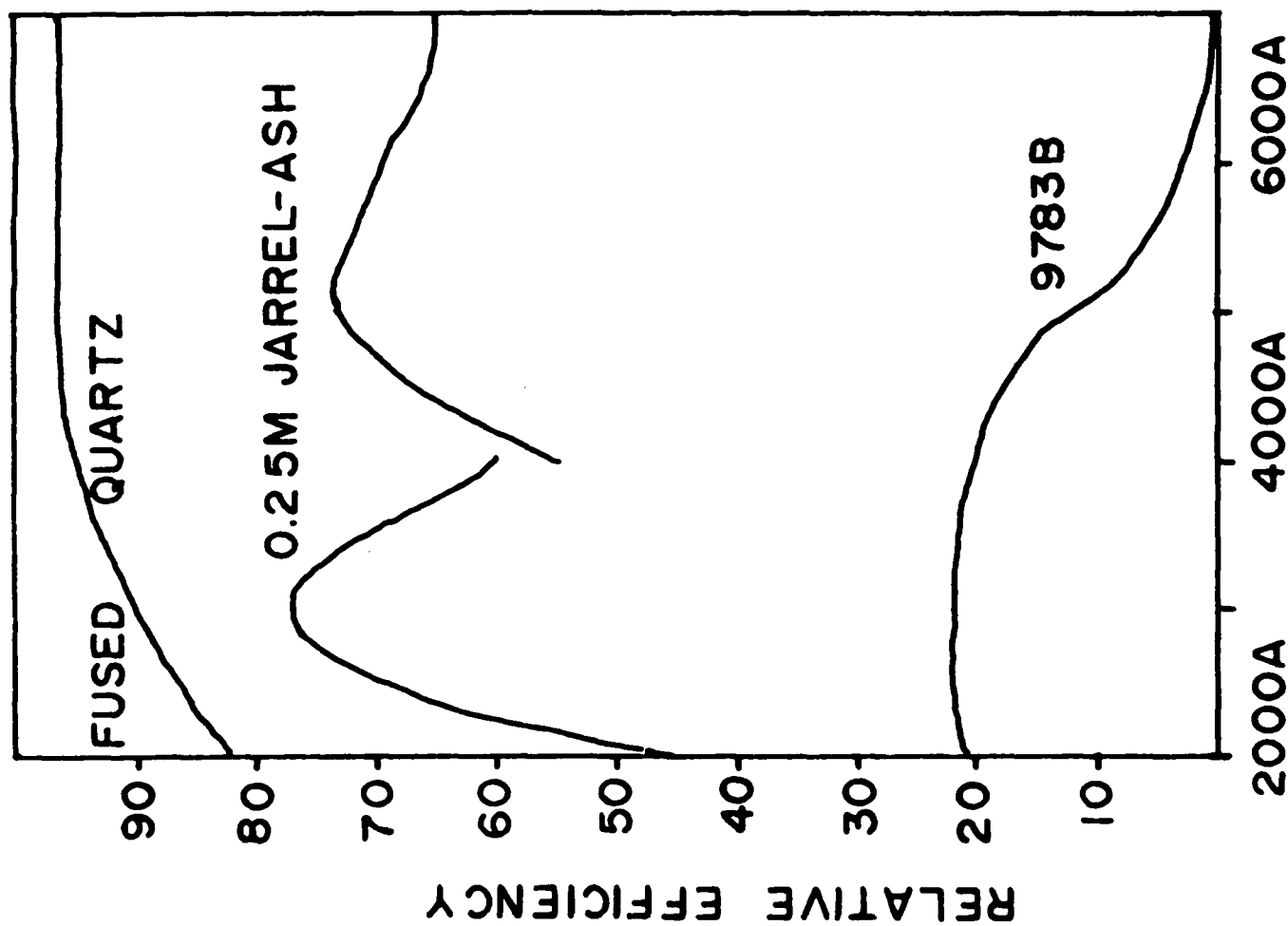
Figure 15. Relative efficiency of detector system for the various elements.
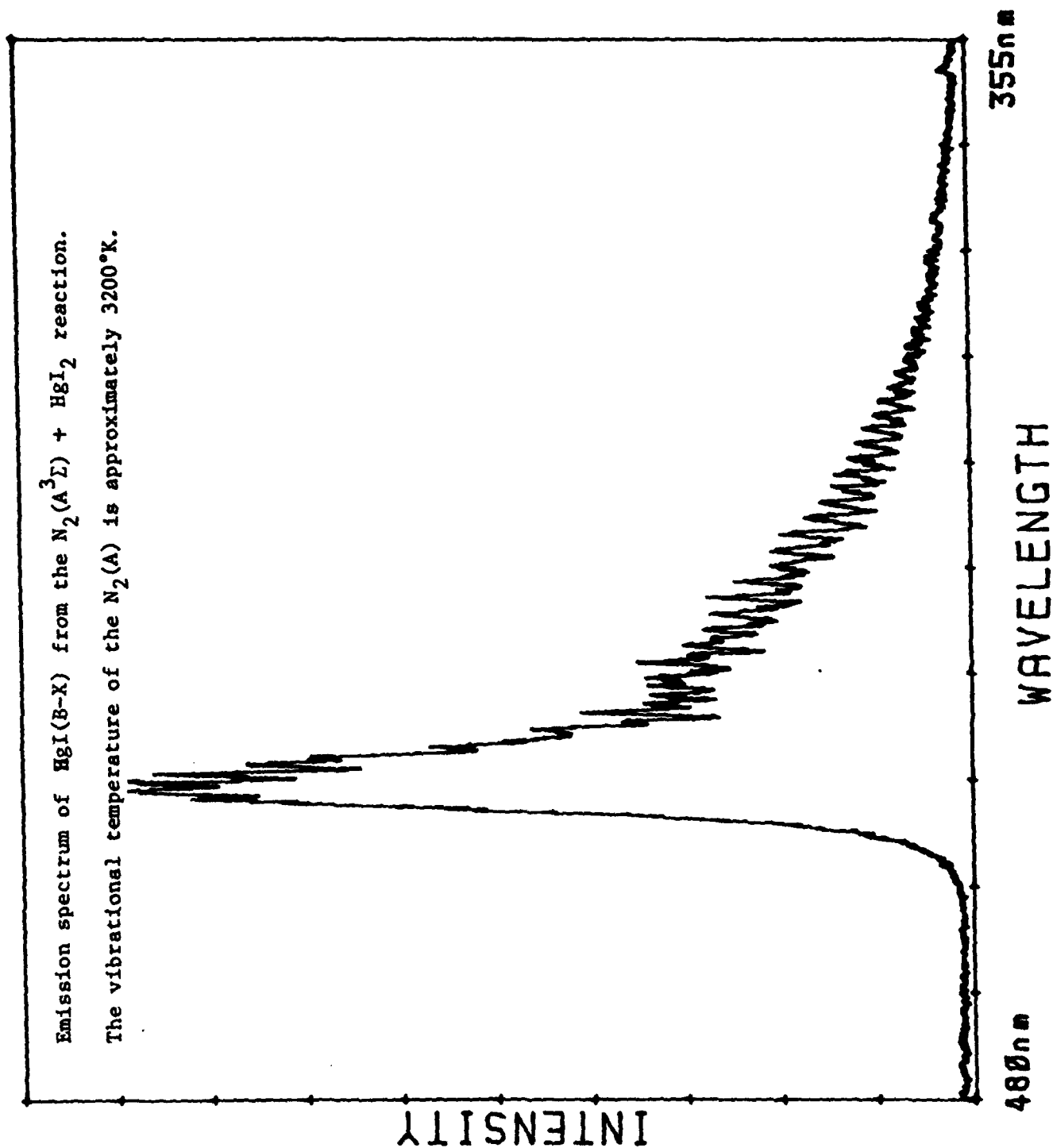
Figure 16a. HgI(B-X) fluorescence in flowing afterglow.

Emission spectrum of HgI(B-X) from the $N_2(A^3\Sigma)$ + $HgI_2$ reaction.

The vibrational temperature of the $N_2(A)$ is approximately 3200°K.

WAVELENGTH

INTENSITY

355nm

480nm
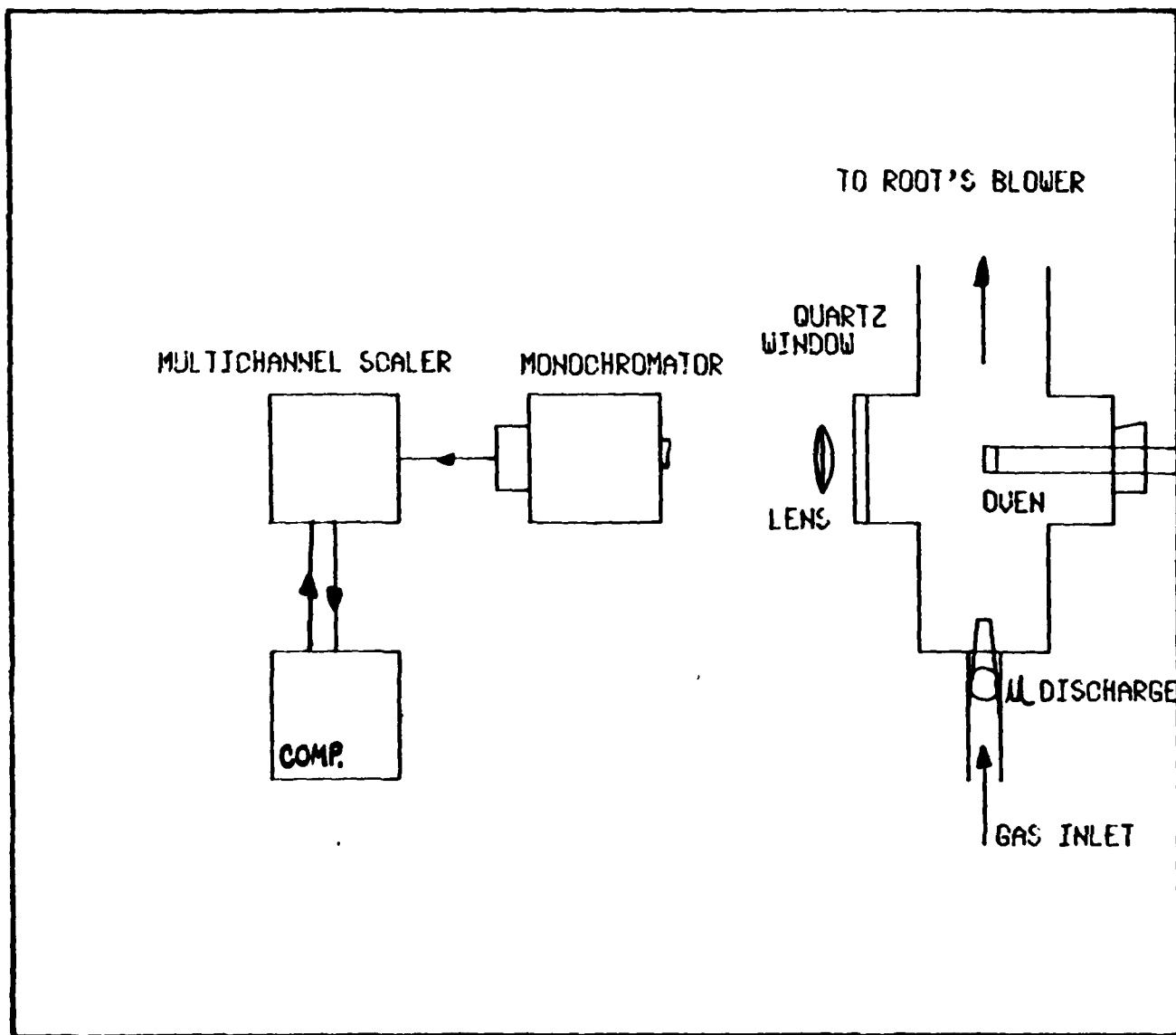
Figure 16B.  Schematic of flowing afterglow apparatus.  The Root's blower
and mechanical pump provide a pumping speed of 540 cfm at
0.2 Torr.
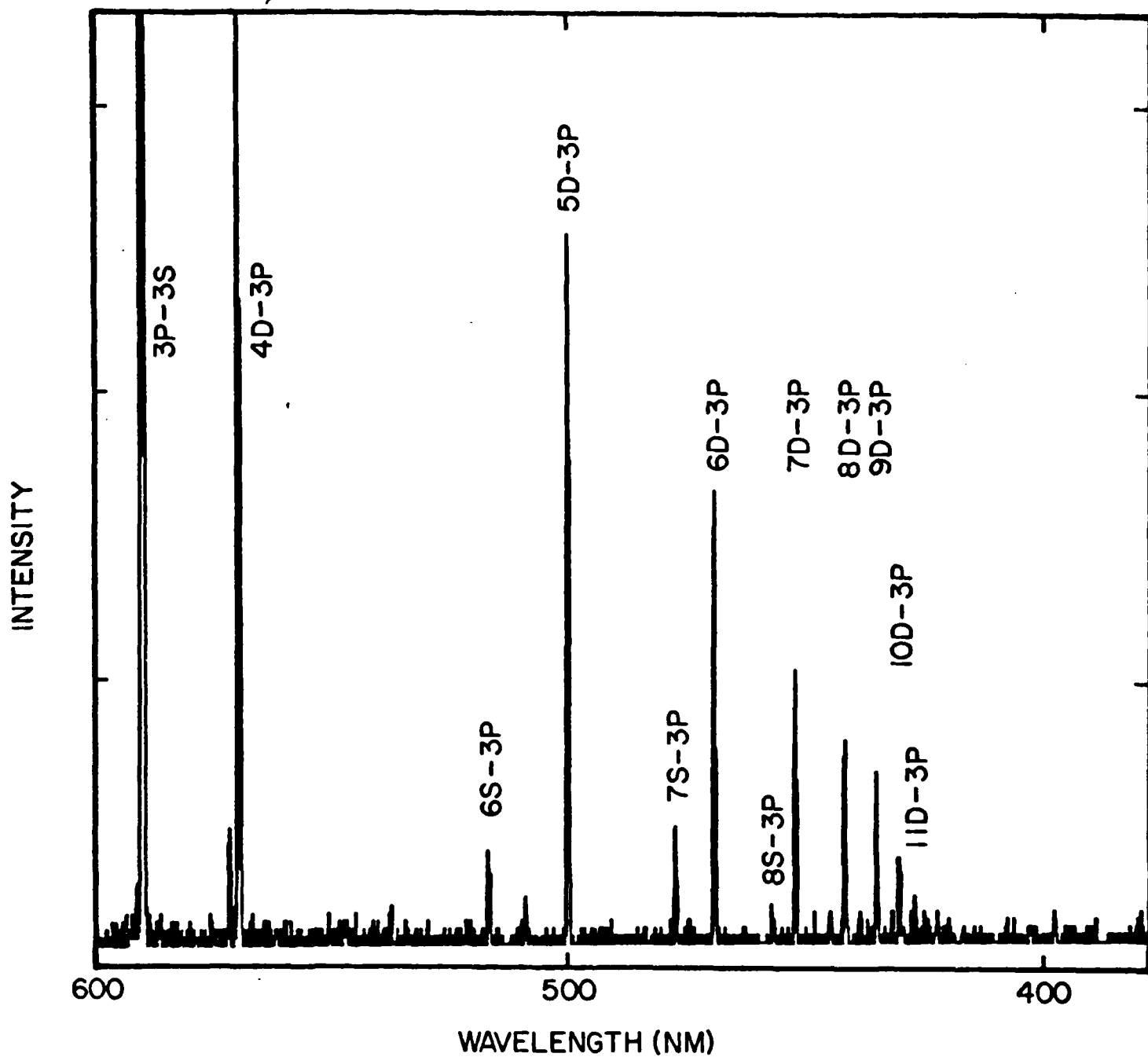
Figure 17. Fluorescence spectrum of Na excited by vibrationally excited $N_2(X^1\Sigma)$ in a flowing $N_2$ afterglow.
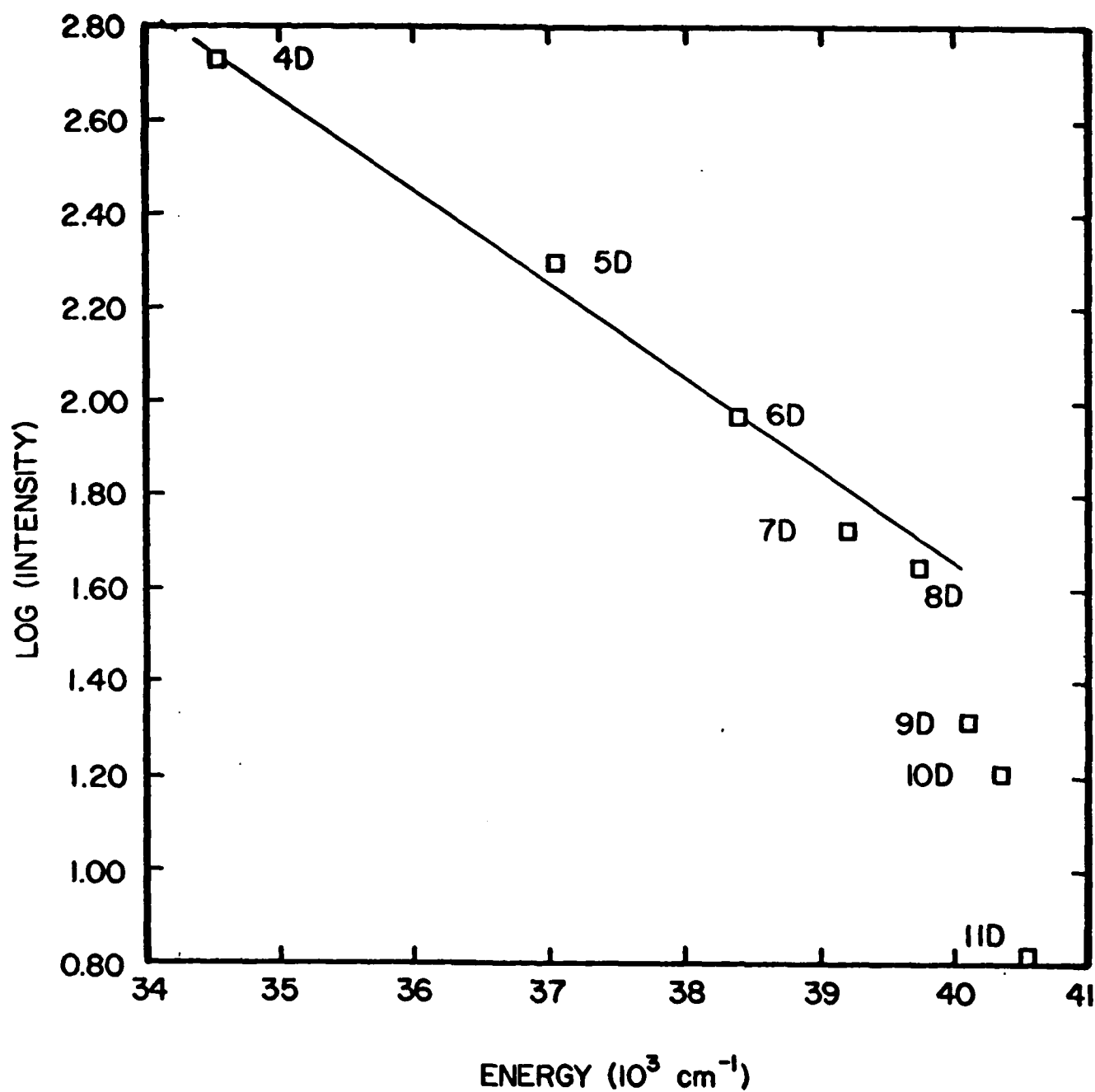
Figure 18. Plot of log (intensity) vs energy of sodium nD states. The straight line yields an excitation temperature of 3100°K.
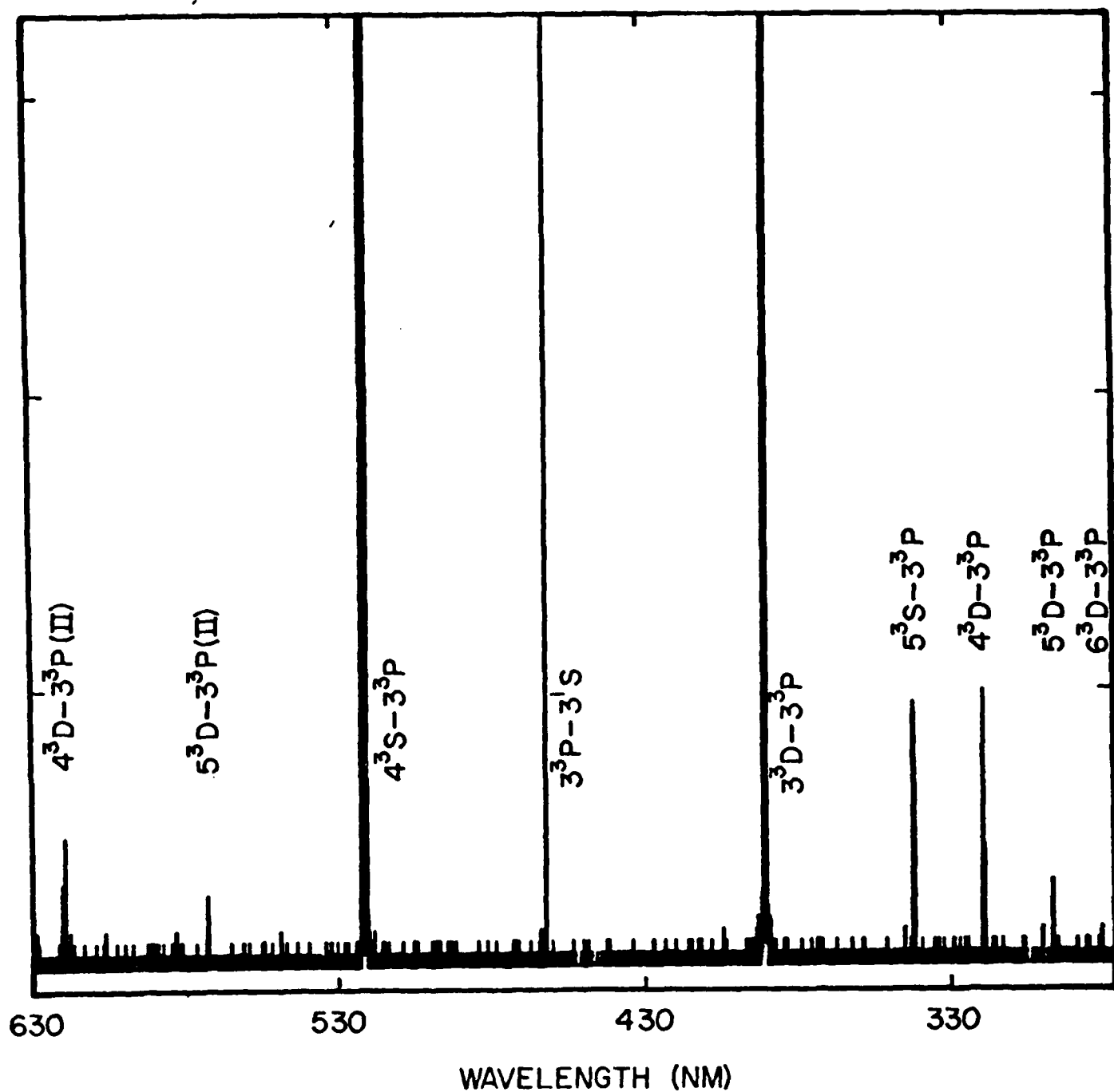
Figure 19.  Fluorescence spectrum of Mg excited by vibrationally excited
$(N_2(A^3\Sigma)$ in a flowing nitrogen afterglow.
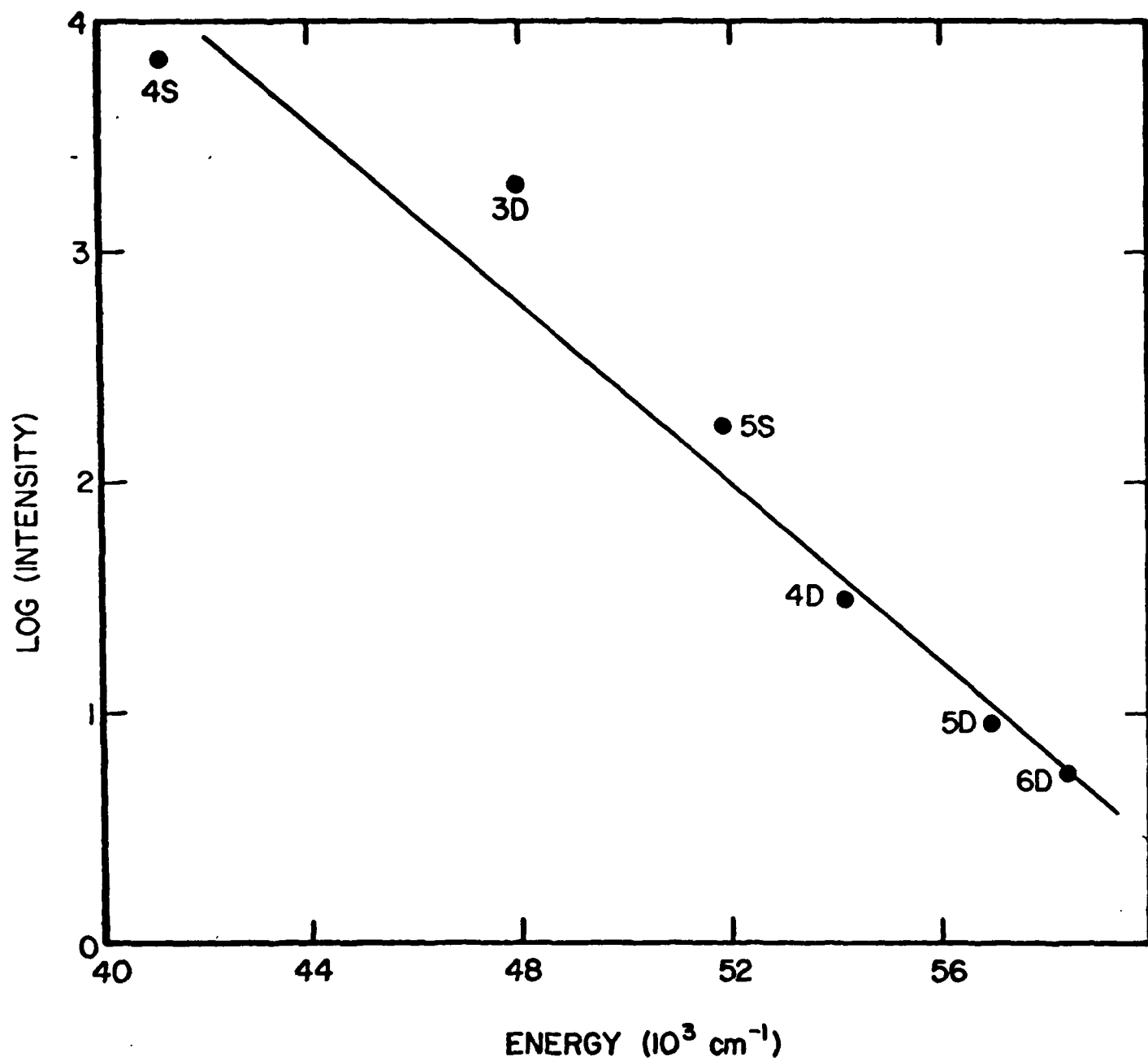
Figure 20.  Plot of log (intensity) vs energy of magnesium nS and nD states.
The straight line yields an excitation temperature of 3100°K.
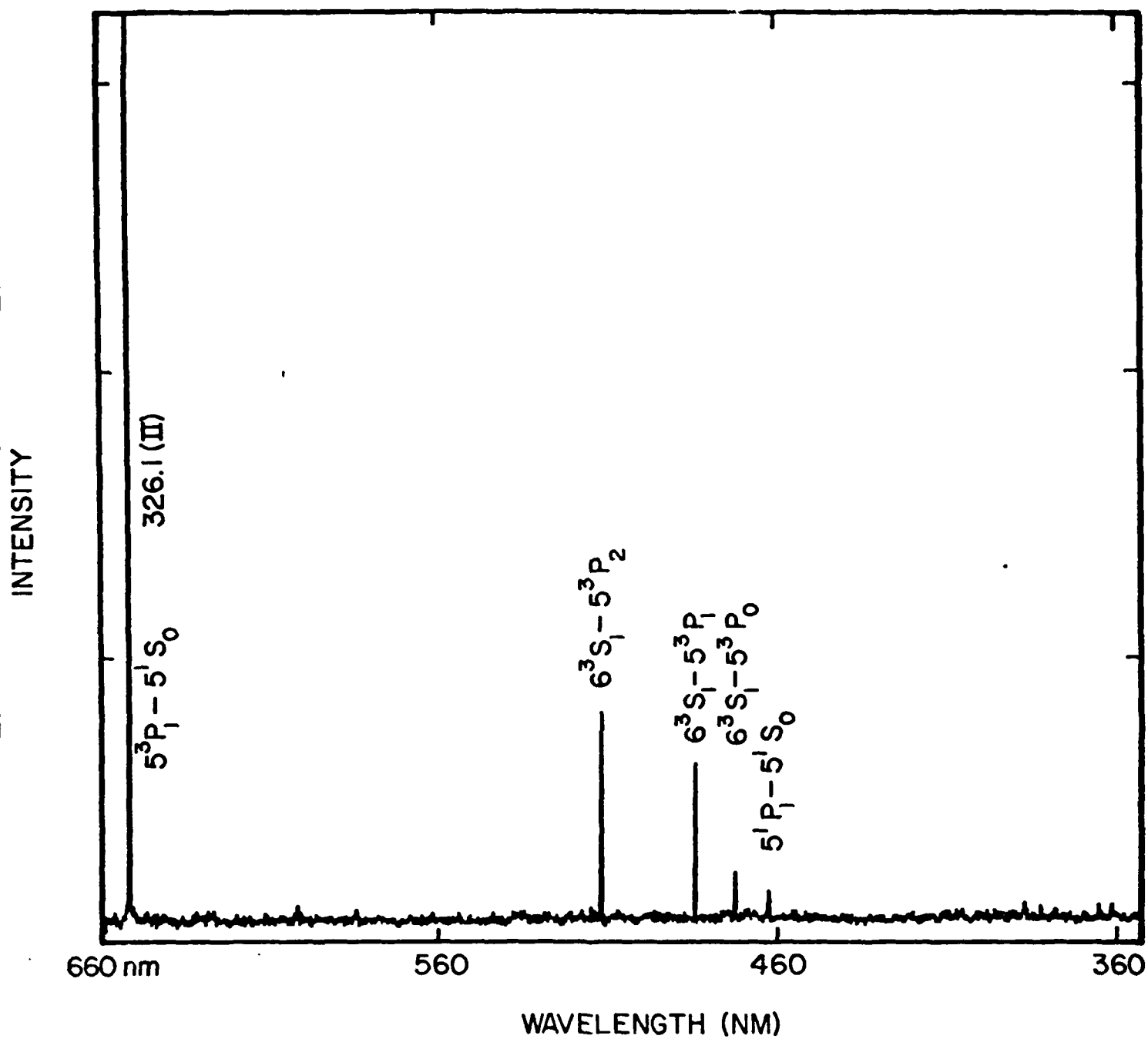
Figure 21. Fluorescence spectrum of Cd excited by vibrationally excited $N_2(A^3\Sigma)$ in flowing nitrogen afterglow.
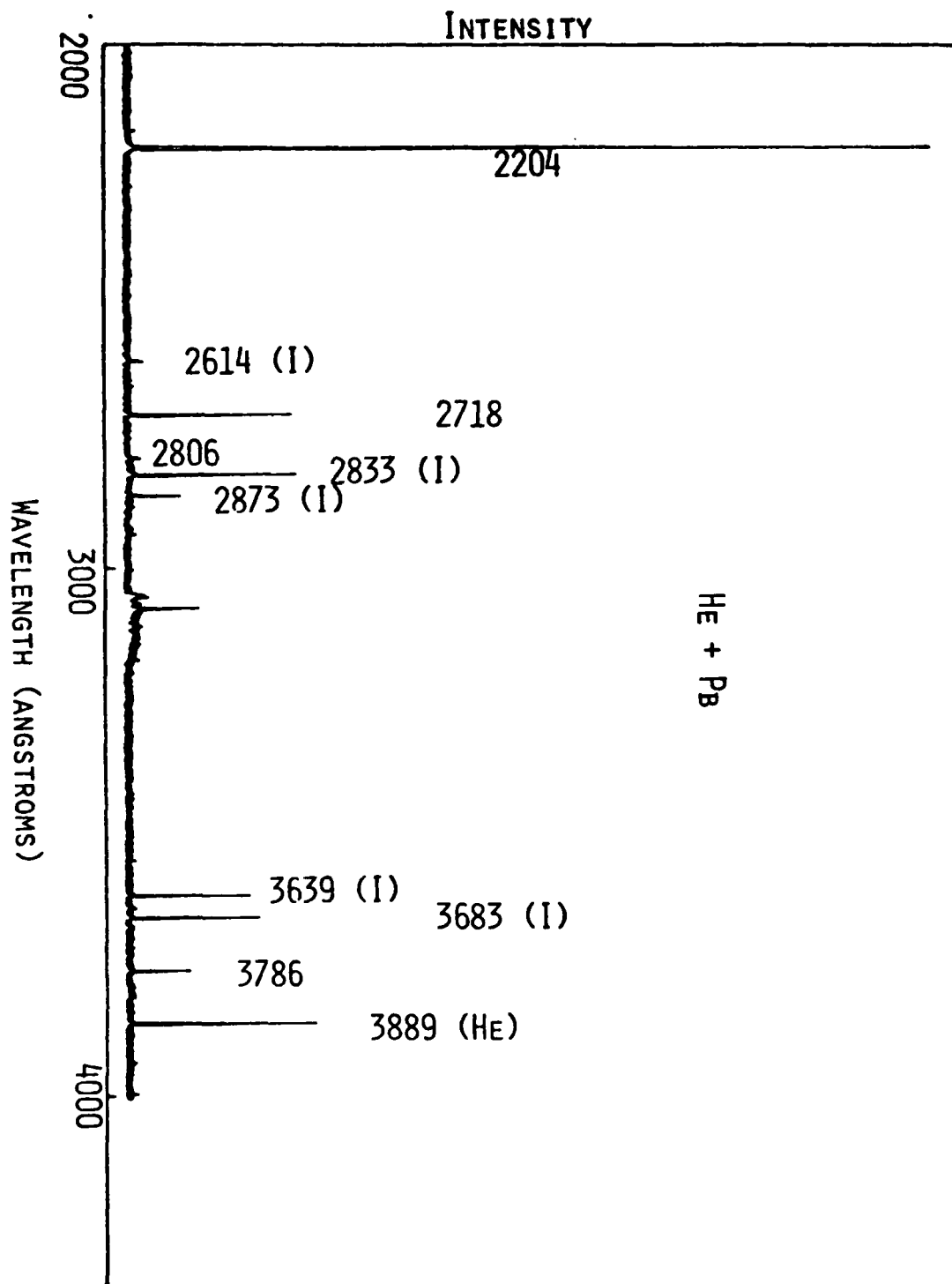
Figure 22a. Fluorescence spectrum of Pb excited by metastable helium in afterglow. The emission is principally from Pb$^+$.
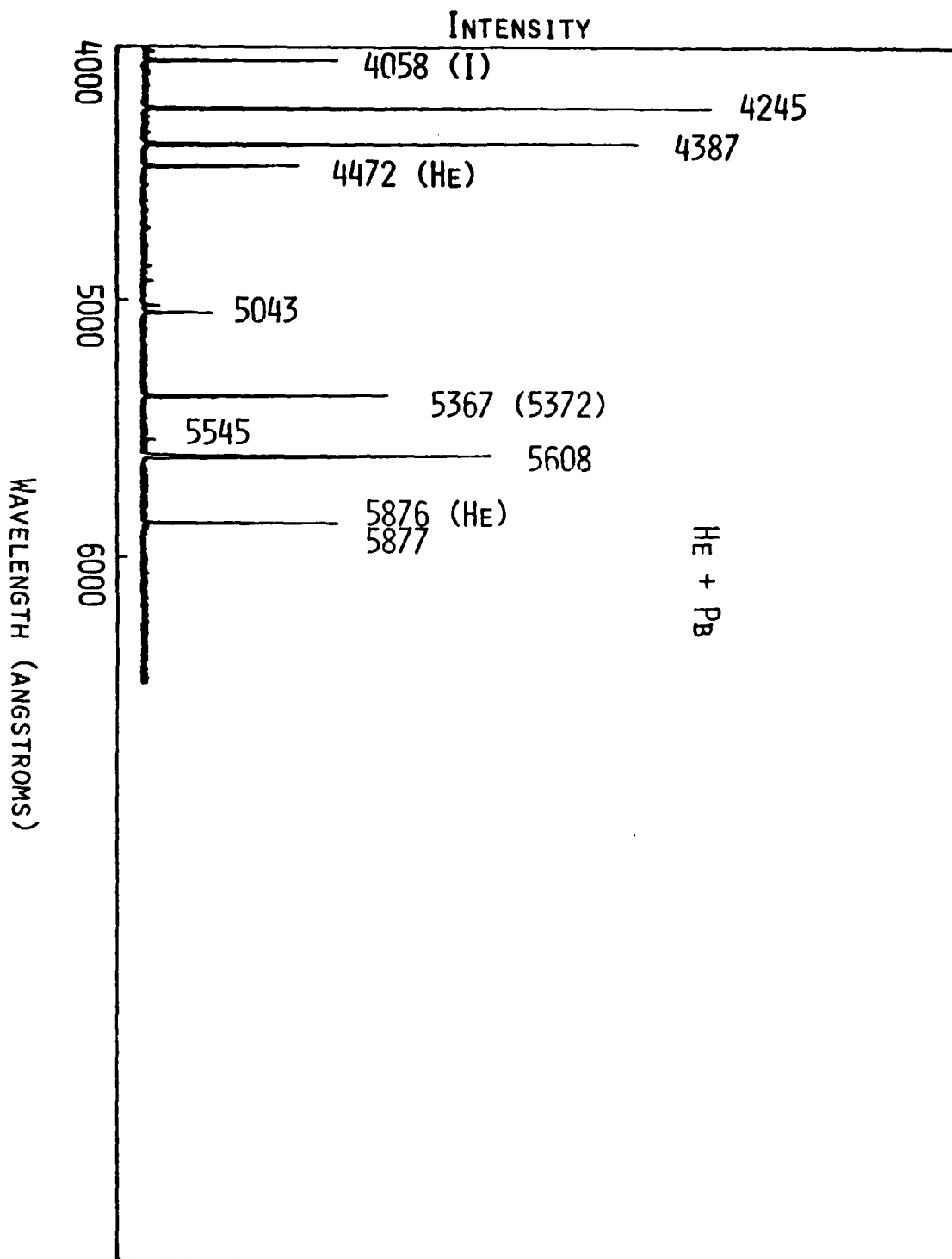
Figure 22b. Fluorescence spectrum of Pb excited by metastable helium in afterglow. The emission is principally from Pb+.
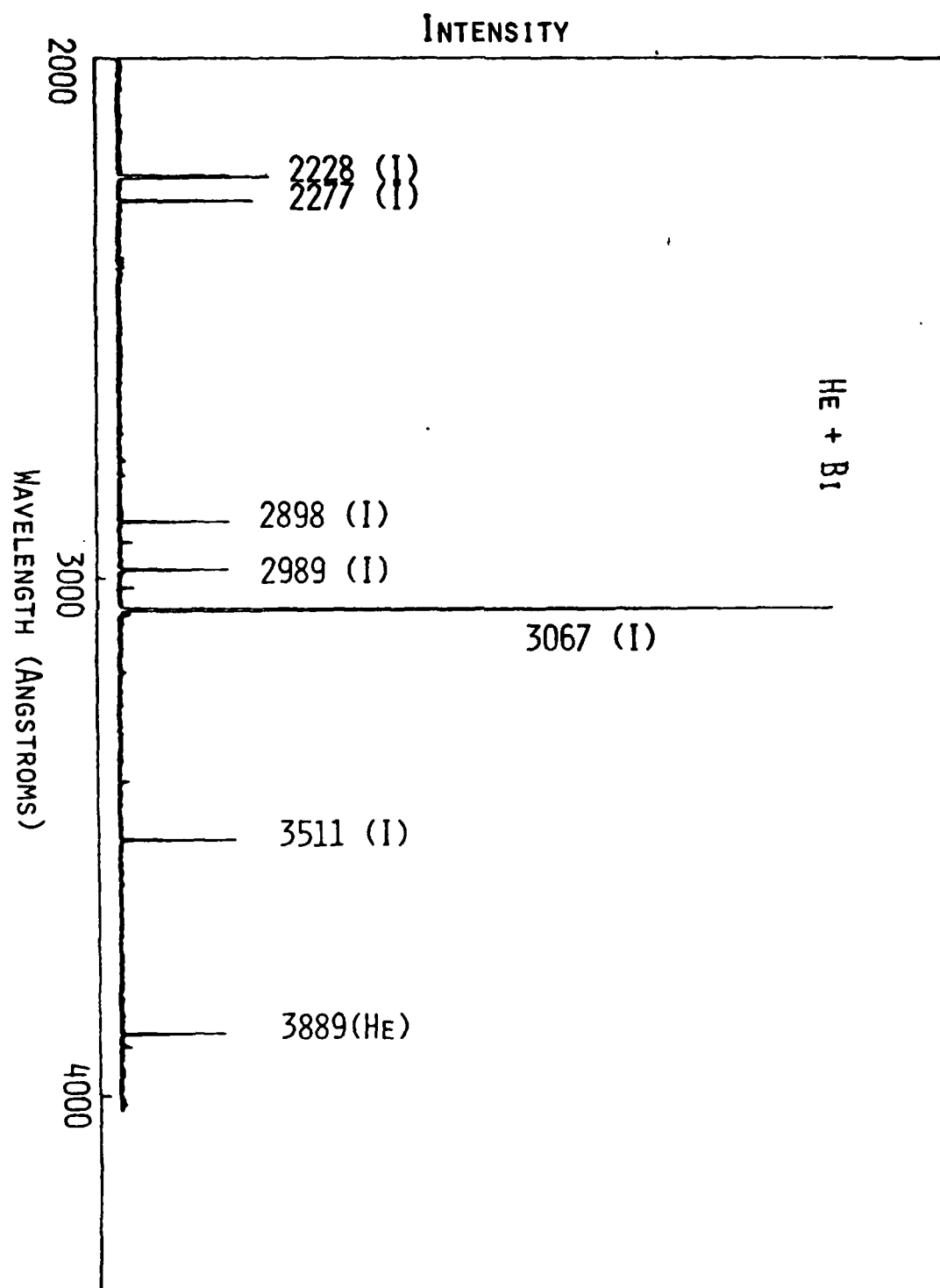
Figure 23a. Fluorescence spectrum of Bi excited by metastable helium. The emission is principally from Bi$^+$.
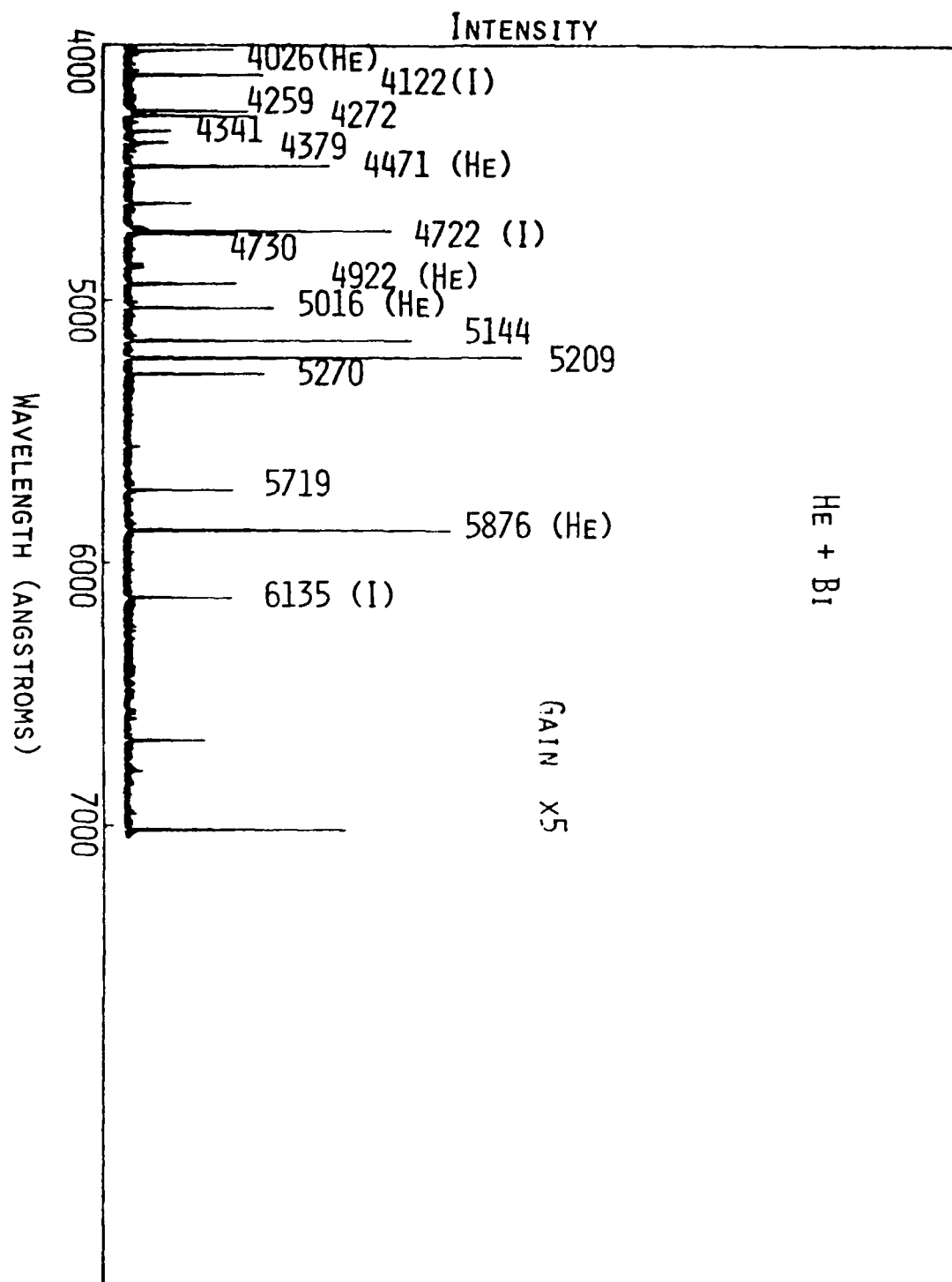
Figure 23b. Fluorescence spectrum of Bi excited by metastable helium. The emission is principally from Bi$^+$.
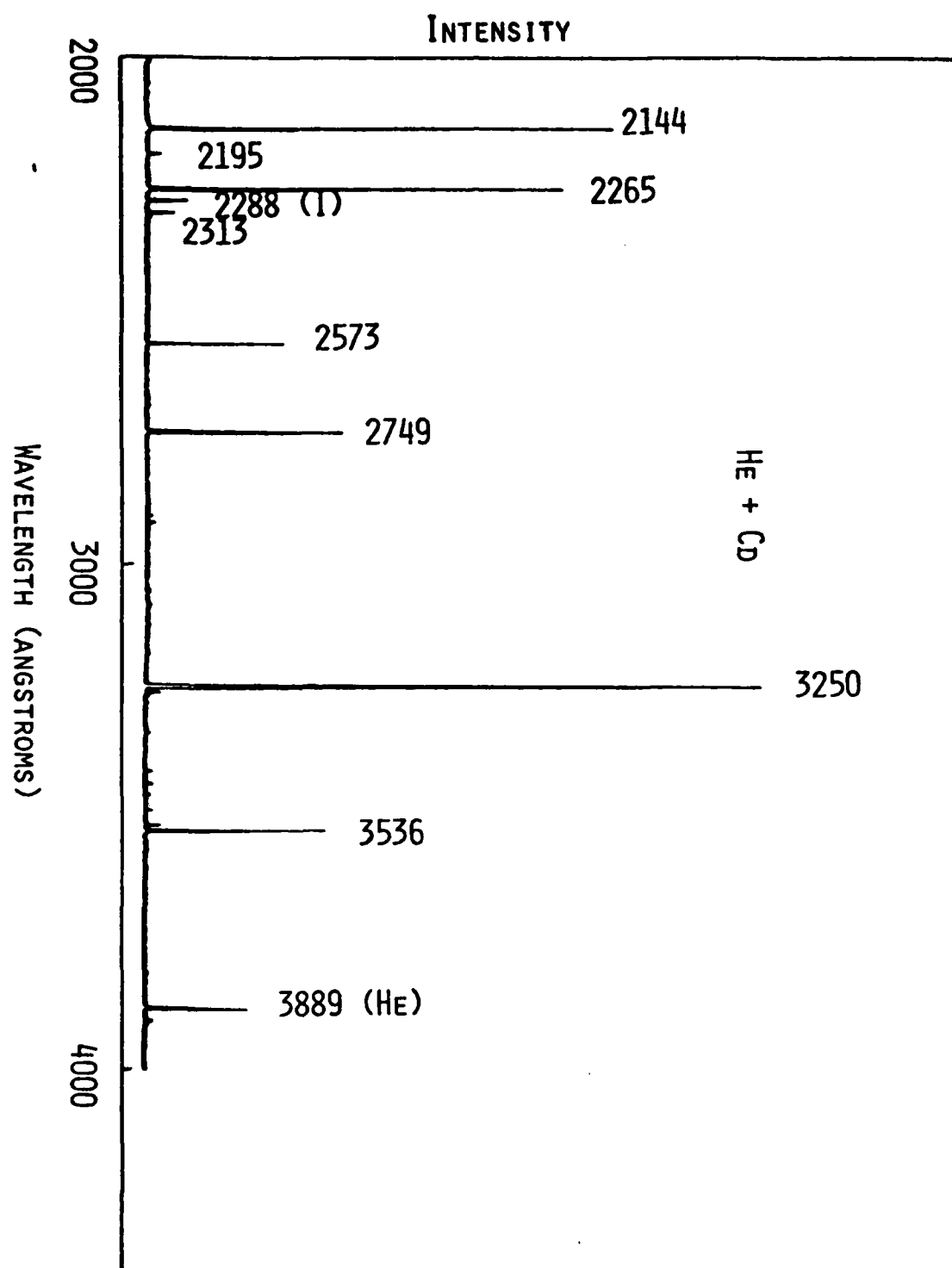
Figure 24a.  Fluorescence from Cd excited by metastable helium. The emission is principally from $Cd^+$.
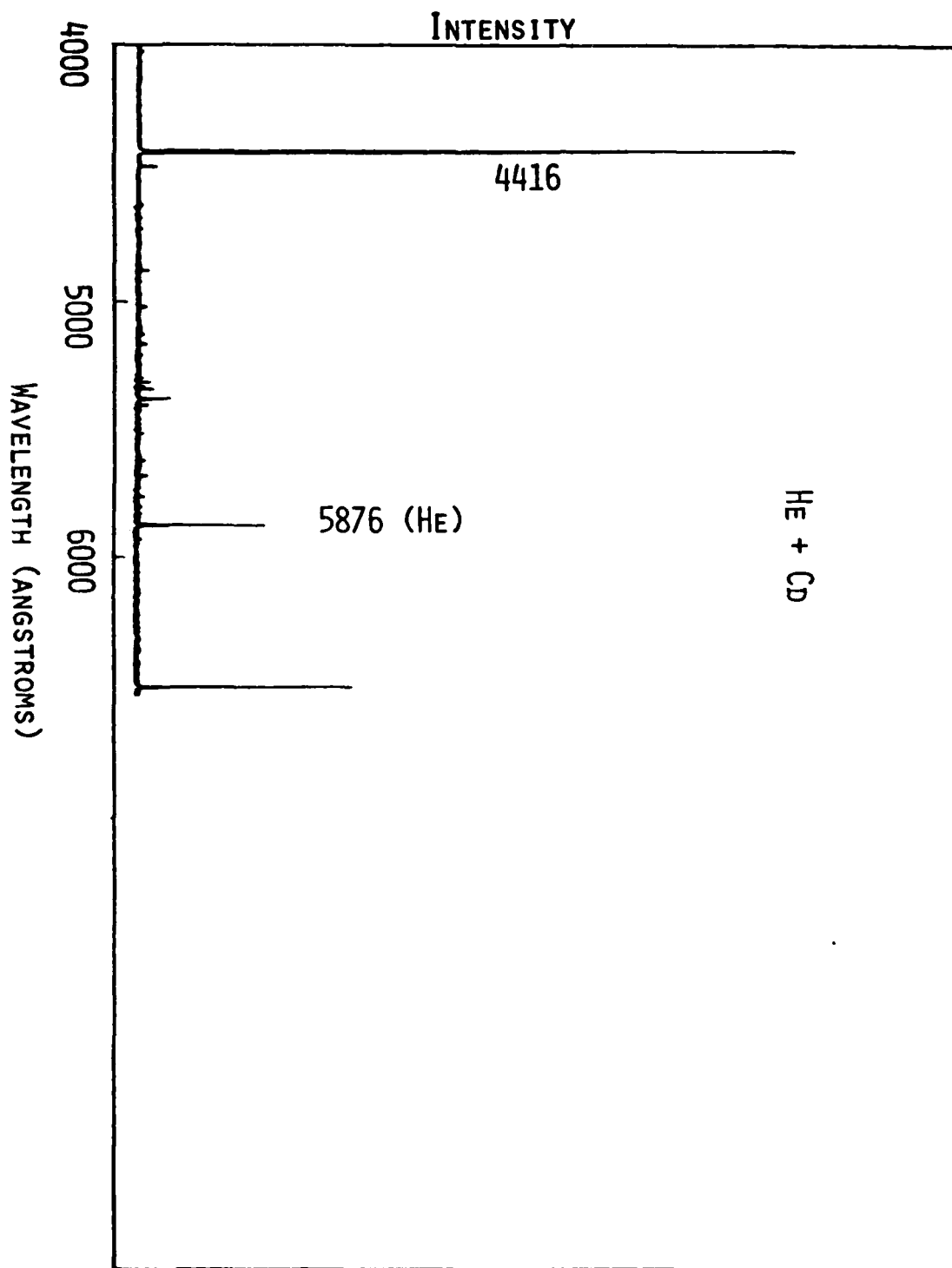
Figure 24b.   Fluorescence from Cd excited by metastable helium.
The emission is principally from $Cd^+$.
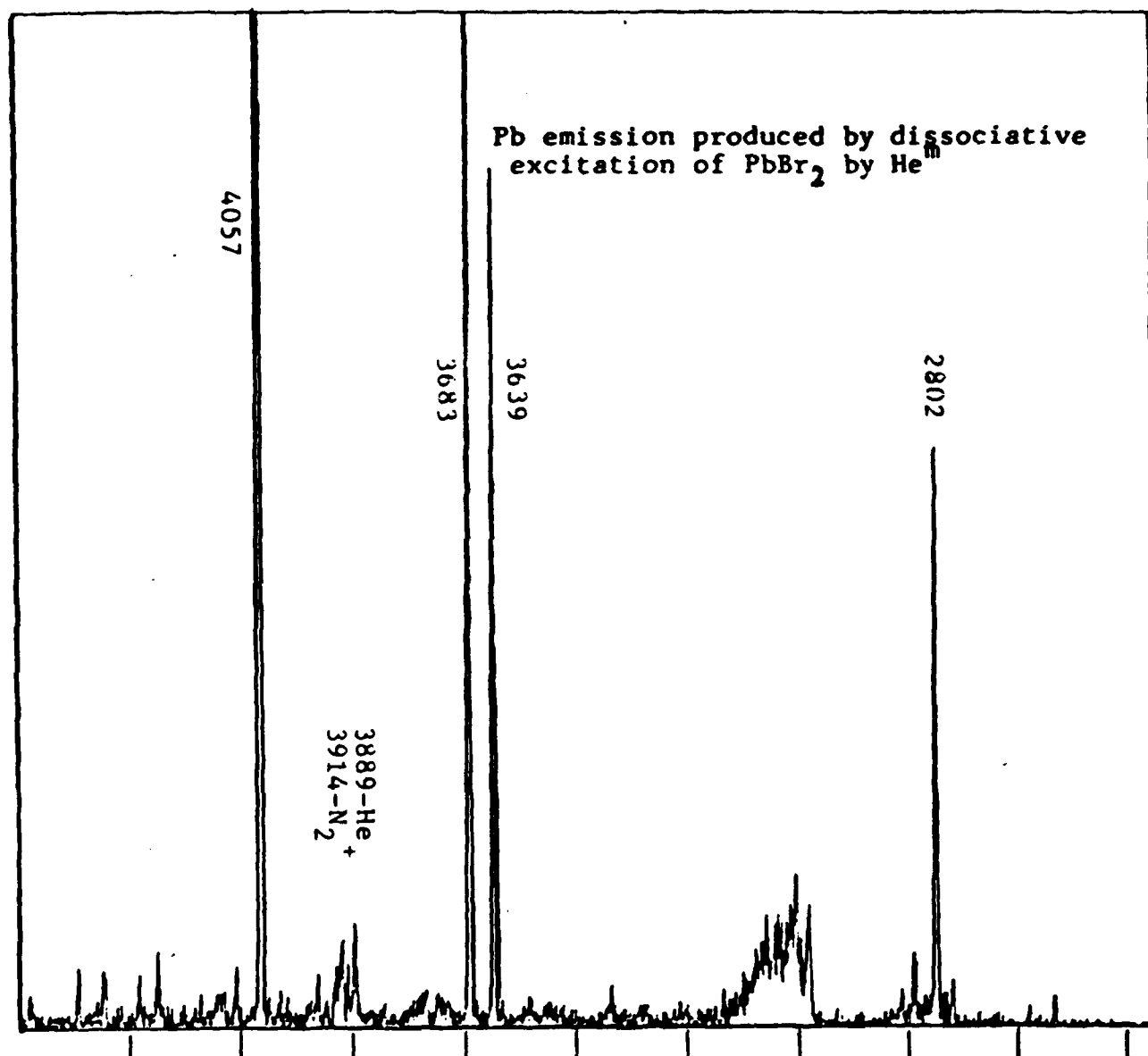
Figure 25. Pb emission produced by dissociative excitation of PbBr$_2$ metastable helium.
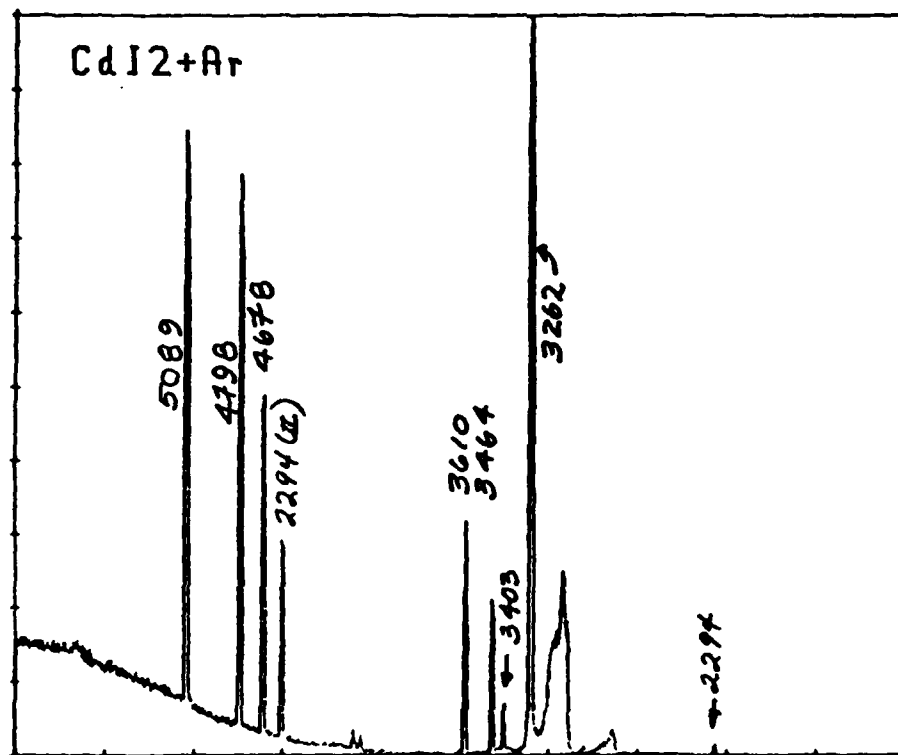
Figure 26. Cd emission produced by dissociative excitation of CdI$_2$ by metastable Argon.
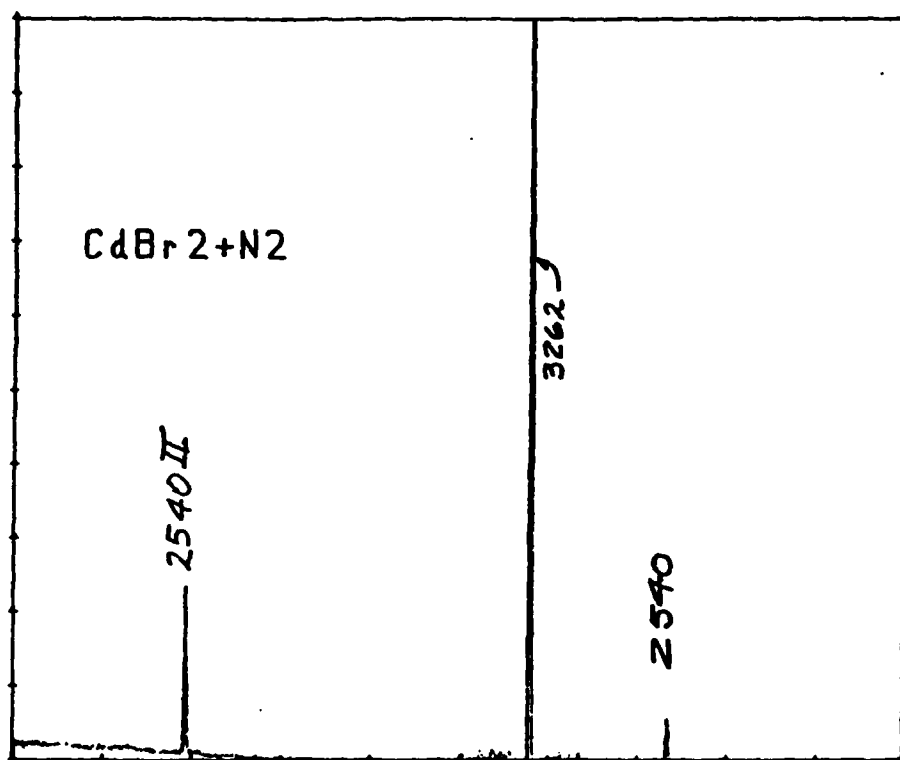
Figure 27. Cd emission produced by dissociative excitation of $CdBr_2$ by metastable $N_2$.

Sb emission produced by dissociative excitation
of $SbI_3$ by Helium metastable atoms in a flowing
afterglow.
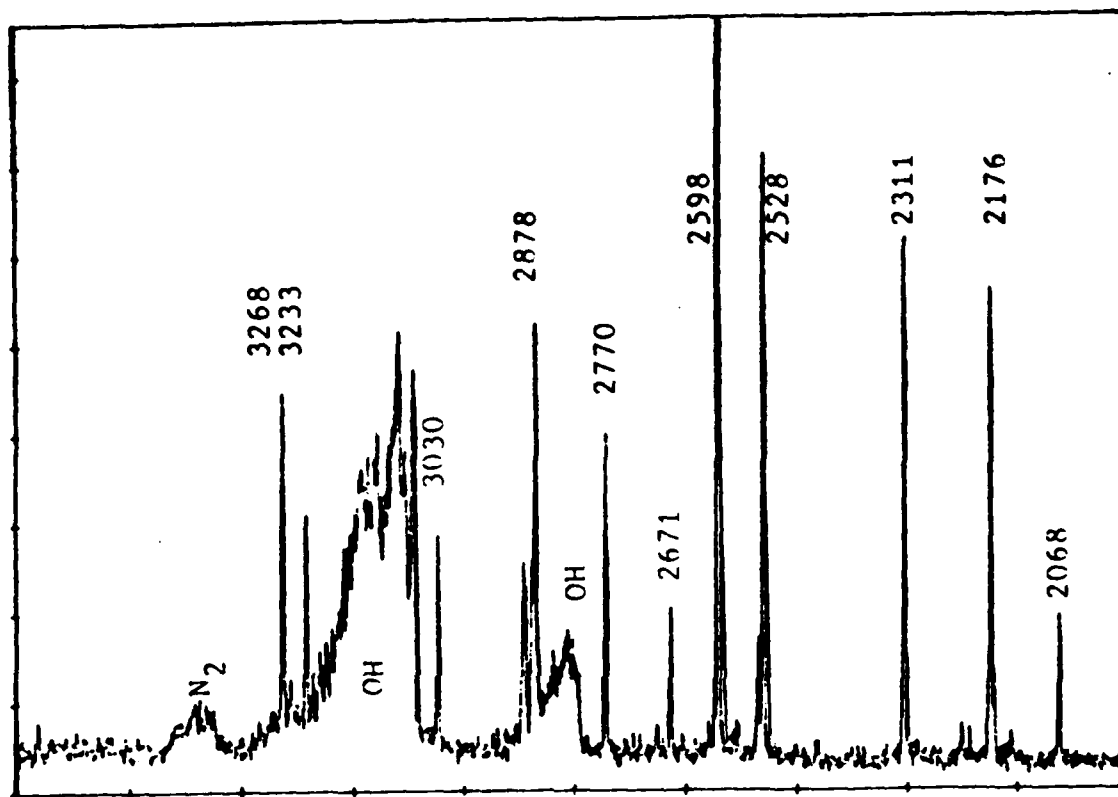


The observed transitions are due to emission from neutral,
atomic Sb and are transitions to the ground state or low
lying metastable levels.

The levels and transitions are shown below:

| WAVELENGTH | Upper level Energy (eV) | Transition |
|---|---|---|
| 3267.5 | 5.82 | $6^2P_{1/2} - 5^4P_{1/2}$ |
| 3232.5 | 6.12 | $6^2P_{3/2} - 5^4P_{3/2}$ |
| 3029.8 | 6.12 | $6^2P_{3/2} - 5^4P_{5/2}$ |
| 2877.9 | 5.36 | $6^4P_{1/2} - 5^2D_{3/2}$ |
| 2769.95 | 5.69 | $6^4P_{3/2} - 5^2D_{3/2}$ |
| 2670.64 | 5.69 | $6^4P_{3/2} - 5^2D_{5/2}$ |
| 2598 | 5.98-5.82 | $6^4P_{1/2} - 5^2D_{3/2}$ |
| 2528 | 6.12 | $6^4P_{3/2} - 5^2D_{5/2}$ |
| 2311.47 | 5.36 | $6^4P_{1/2} - 5^4S_{3/2}$ |
| 2175.81 | 5.69 | $6^4P_{3/2} - 5^4S_{3/2}$ |
| 2068.3 | 5.98 | $6^4P_{3/2} - 5^4S_{3/2}$ |

Figure 28.  Sb emission produced by dissociative excitation of $SbI_3$
by metastable helium.
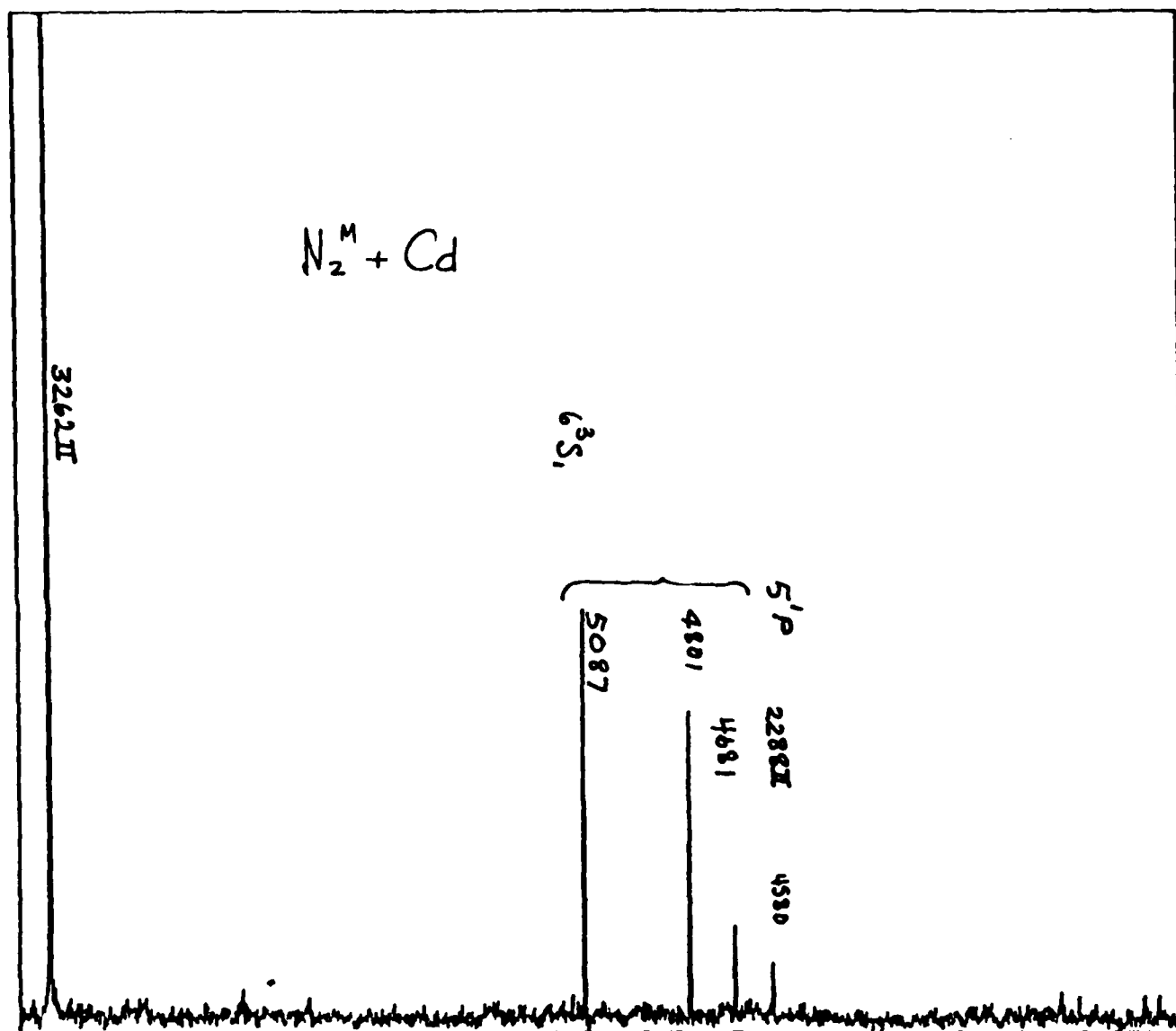
Figure 29. Cd emission produced by energy transfer collisions of Cd with vibrationally excited $N_2(A^3\Sigma)$.
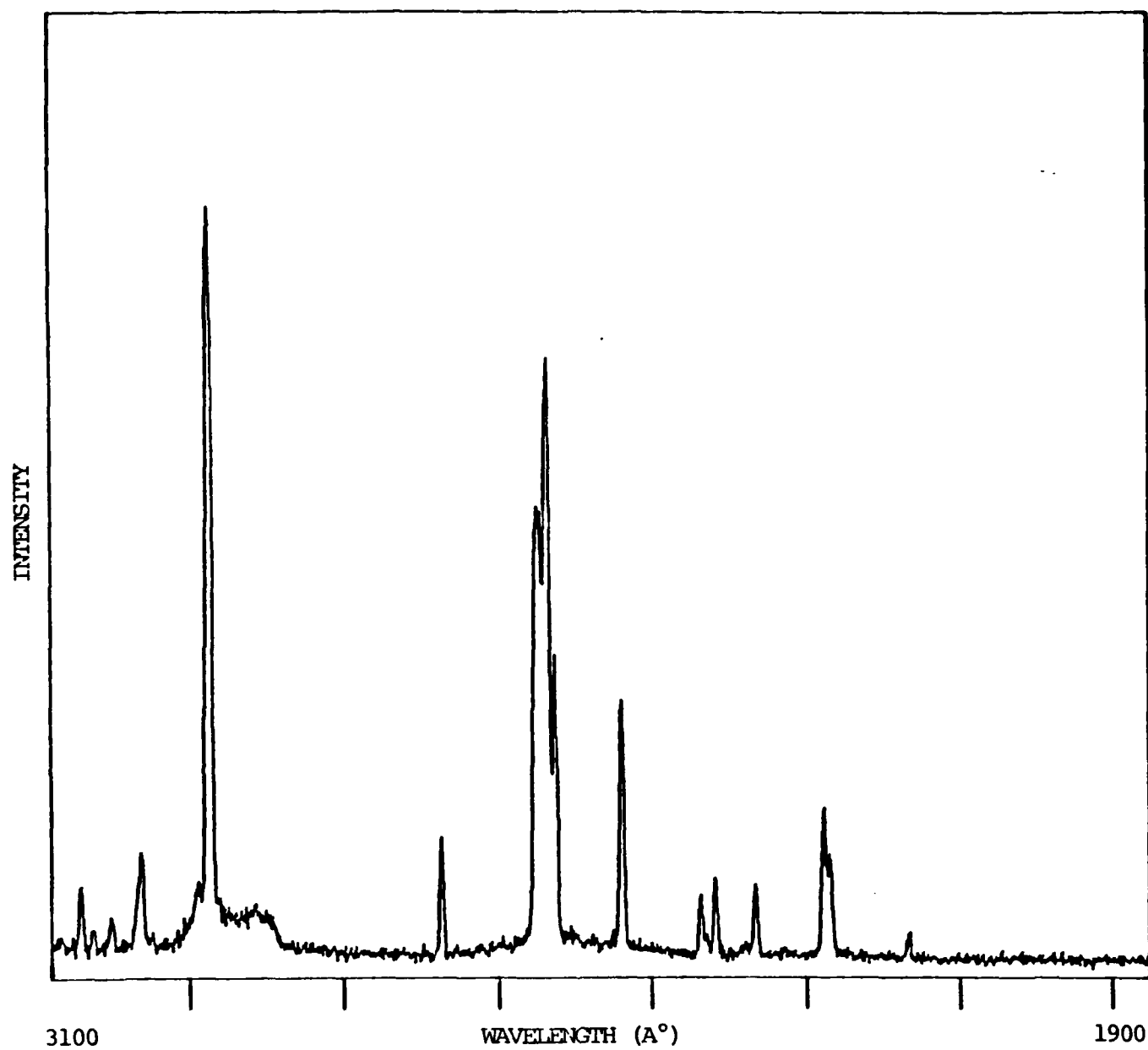
INTENSITY

3100                               WAVELENGTH (A°)                          1900

Figure 30a. Emission spectrum produced by $SiH_4$ + metastable helium.
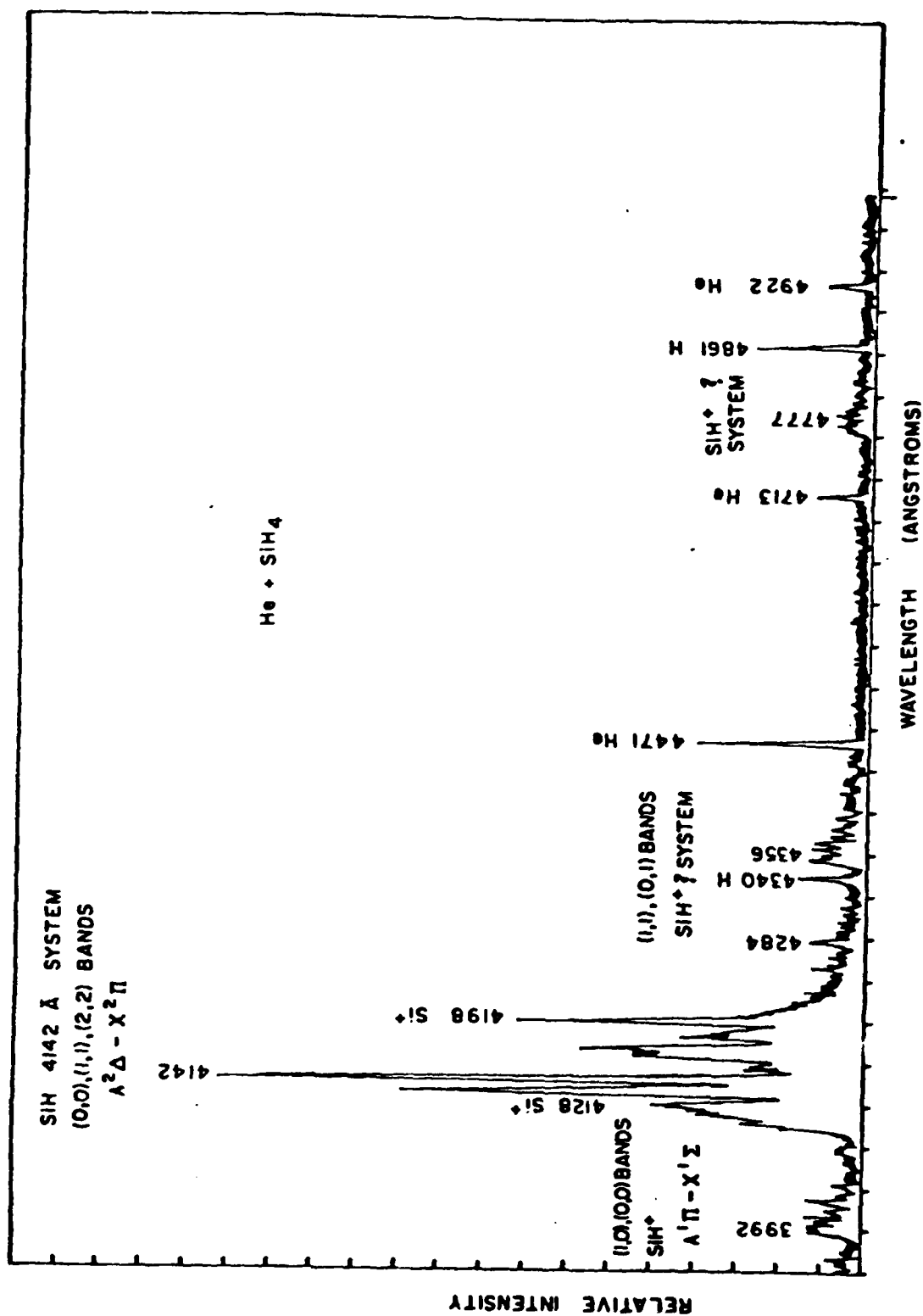
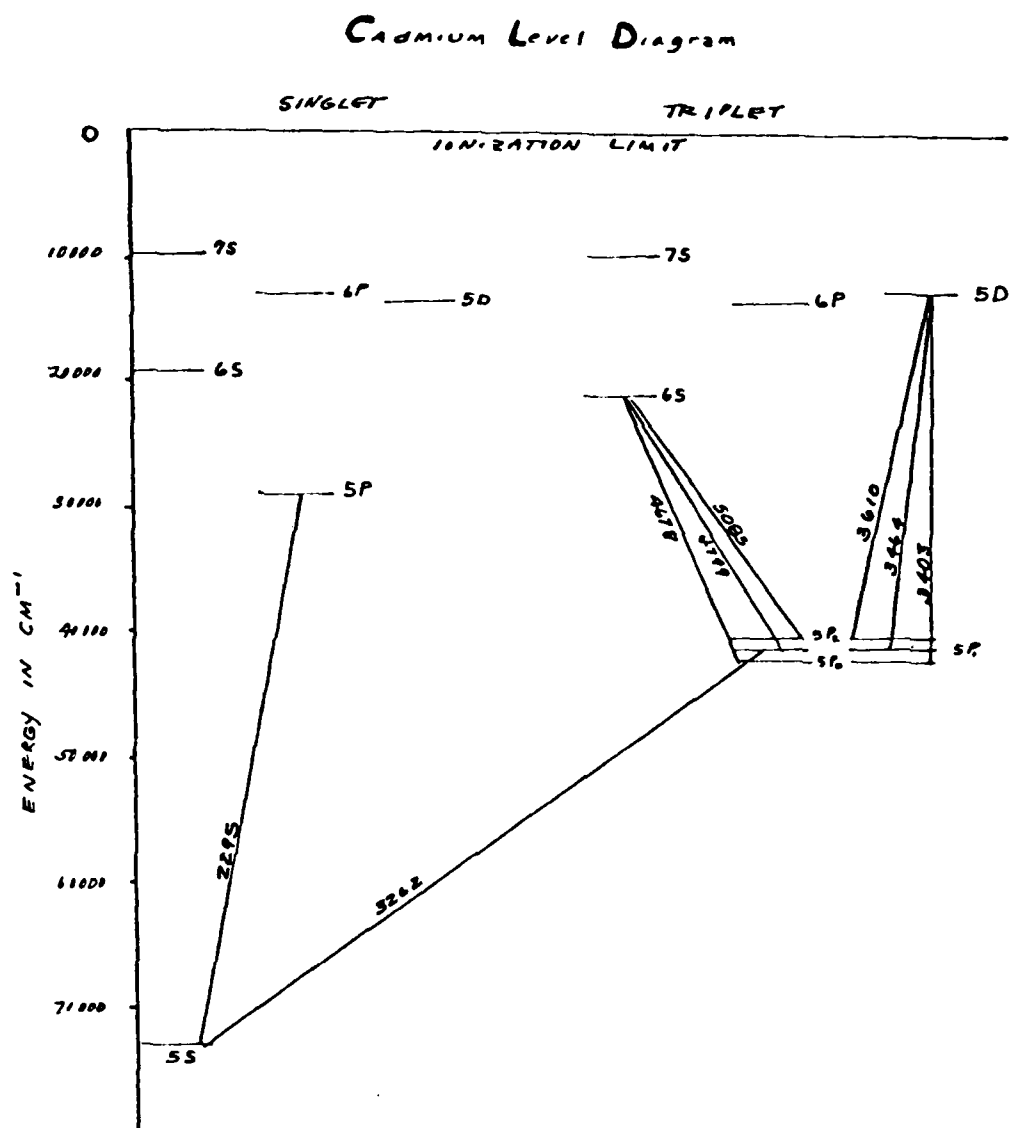Figure 30b.  Emission spectrum produced by $SiH_4$ + metastable helium.

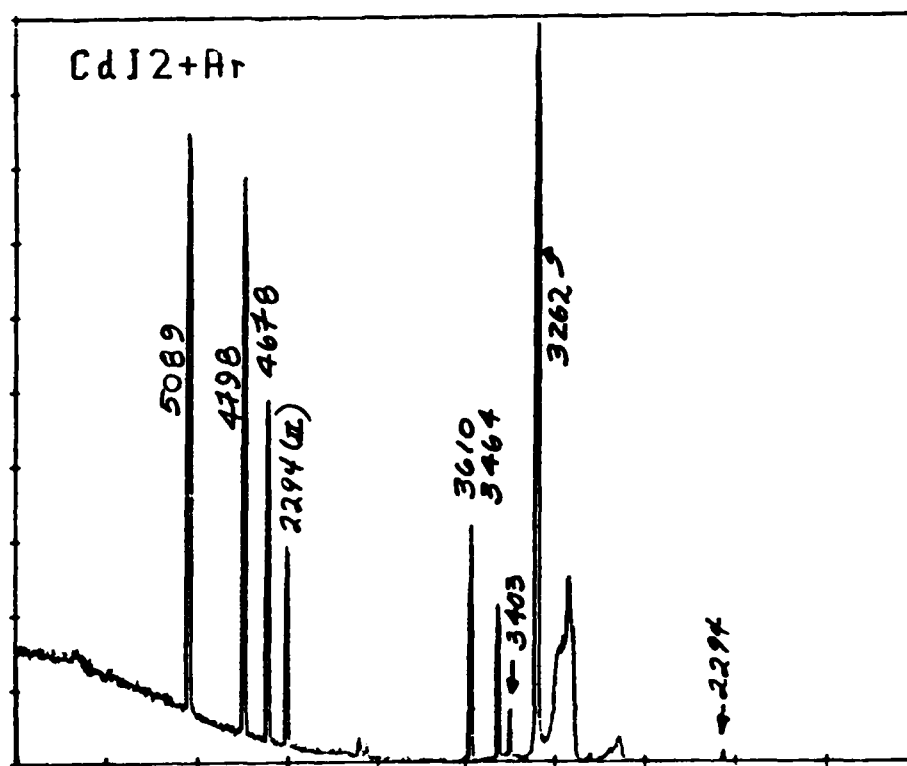Figure 31.   Partial energy level diagram of cadmium.

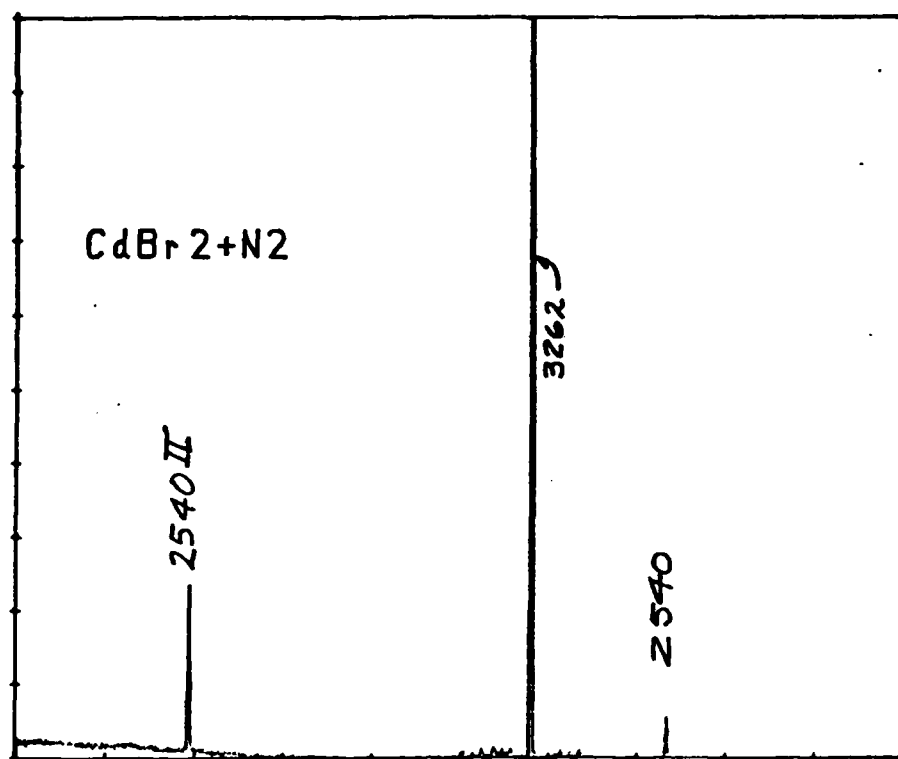Figure 32. Fluorescence produced by $CdI_2$ + metastable argon.
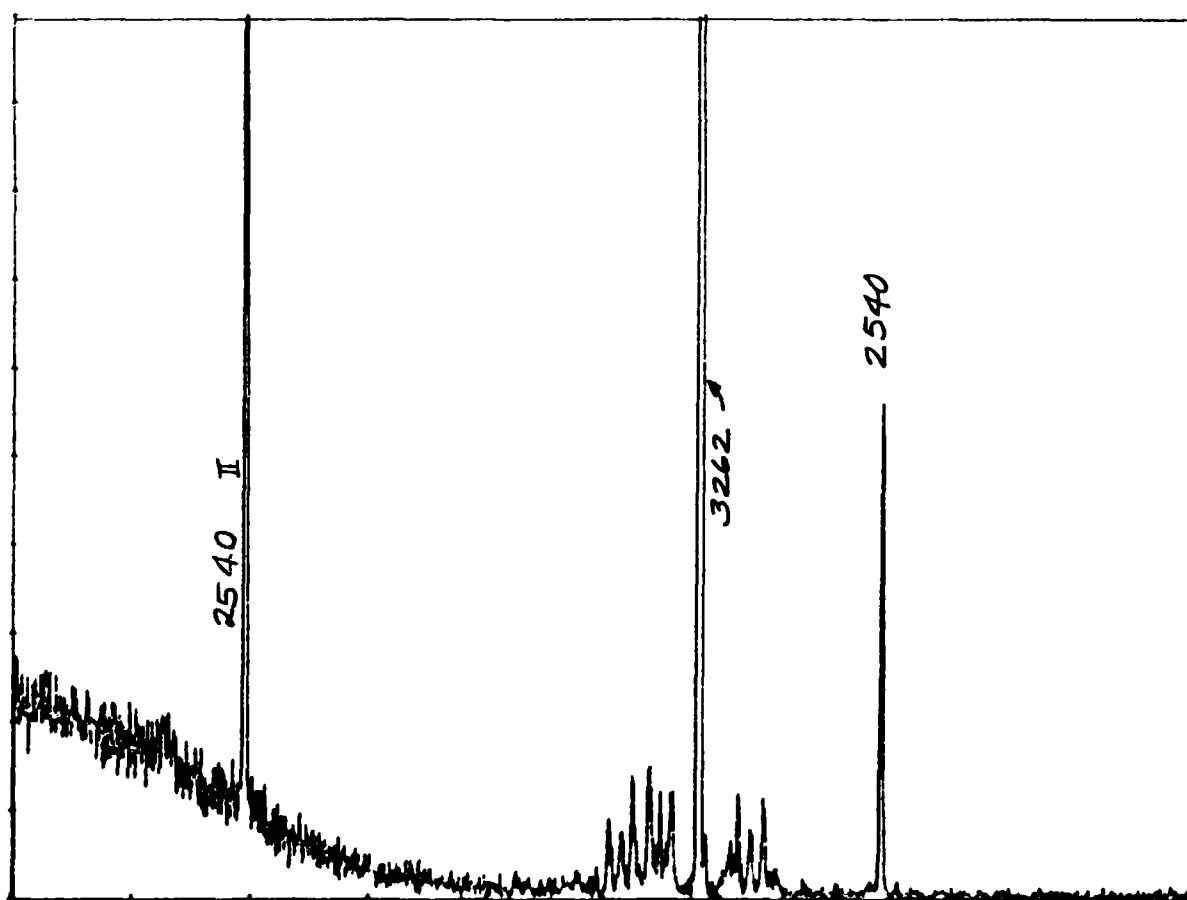
Figure 33a.  Fluorescence produced by $CdBr_2$ + metastable $N_2(A^3\Sigma)$.



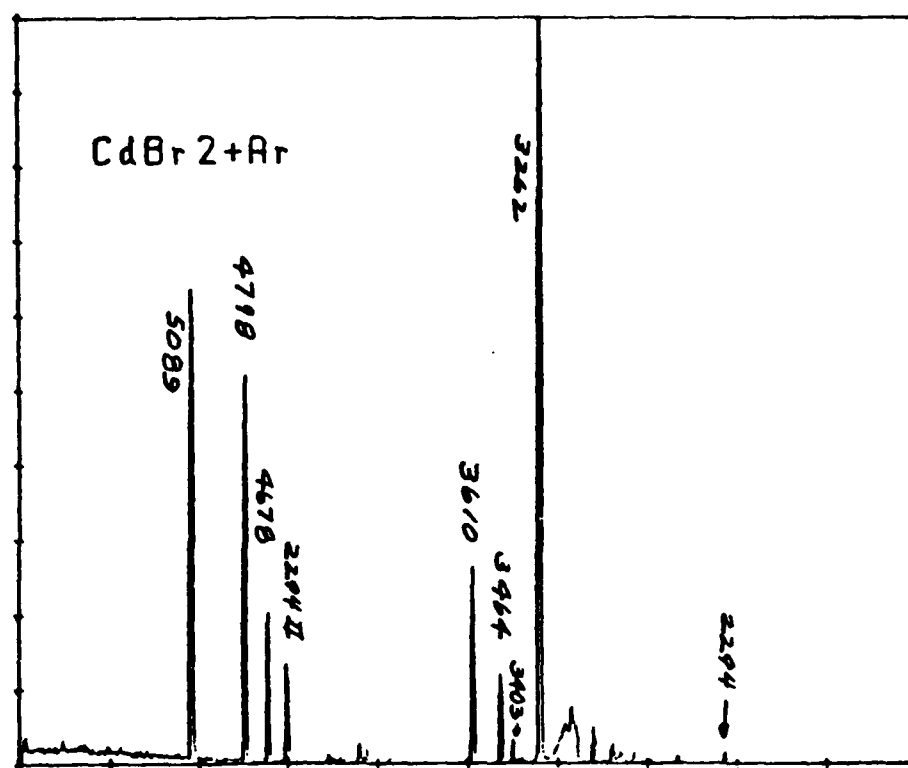Figure 33b.  Fluorescence produced by $CdBr_2$ + metastable $N_2(A^3\Sigma)$.

Figure 34. Fluorescence spectrum produced by $CdBr_2$ + metastable argon.
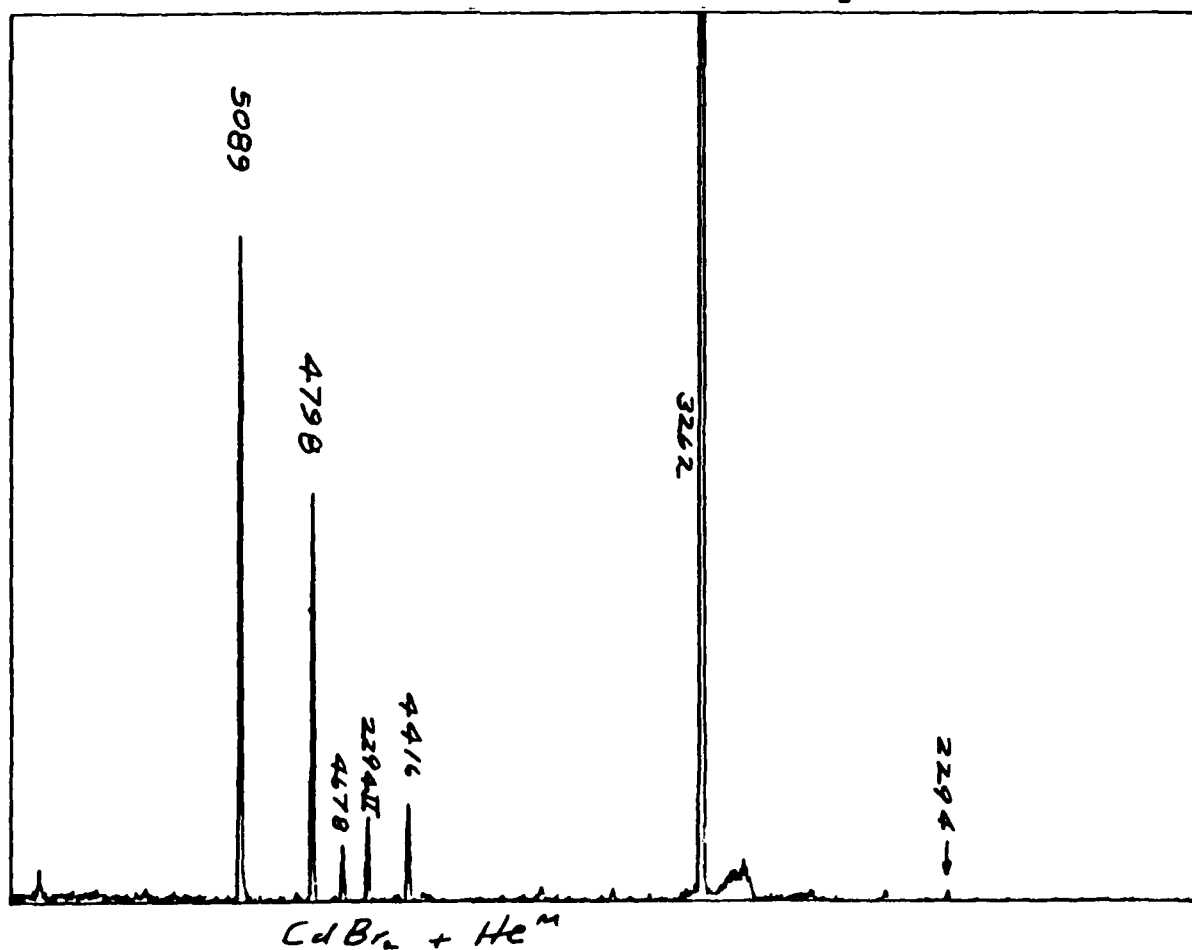


Figure 35. Fluorescence spectrum produced by $CdBr_2$ + metastable helium.

# END

# FILMED

10-85

# DTIC